ORIGINAL PAPER

Syn-exhumation metasomatic glaucophane-phengite-quartz veins formed at moderate pressures: exploring the control of fO$_2$ and bulk composition on nominally HP metamorphic assemblages

T. A. Ducharme[1] · D. A. Schneider[1] · B. Grasemann[2] · M. Bukała[3] · A. Camacho[4] · K. P. Larson[5] · K. Soukis[6]

Abstract

Veins composed of glaucophane + phengite + quartz cross-cut the high pressure-low temperature (HP-LT) Cycladic Blueschist Unit (CBU) of southern Evia, Greece. The veins exhibit a rheology-dependent distribution within layered metamorphic rock comprising cm-scale intercalations of albite-clinopyroxene metabasalt and schistose quartzite. Strain was accommodated by ductile processes in the quartzite, whereas brittle deformation produced four sets of crack-seal syntaxial veins in the coarser-grained metabasalt. All vein sets are subvertical to steeply-dipping and are oriented at high angles to one another. The geometry of the planar vein walls suggests the veins are mode-I (opening mode) fractures, whose sub-vertical orientations indicate formation during extension. Oxygen isotope thermometry using phengite-quartz pairs provides crystallization temperatures of 315–335 °C. Combined ^{40}Ar/^{39}Ar and *in-situ* ^{87}Rb/^{87}Sr geochronology of vein-hosted phengite and glaucophane indicate crystallization and vein sealing at *c*. 22–23 Ma when the CBU is predicted to be undergoing greenschist facies metamorphism coincident with regional extension. The structural and stable isotope data are likewise consistent with a syn-exhumation extensional setting, and easily reconciled with existing petrological data indicating the CBU sustained prolonged residence near the greenschist-blueschist facies boundary. We propose a model whereby phengite and glaucophane were stabilized at greenschist facies conditions by the elevated α_{SiO2} and fO$_2$ in the fluid parental to the veins. Our data provide strong new evidence for the sensitivity of nominally blueschist facies minerals to bulk system chemistry, supported by thermodynamic modelling evidence from other orogens that such HP-LT minerals may exhibit stability that spans multiple stages of orogenesis.

Keywords Hydrothermal veins · High pressure metamorphism · Metasomatism · Cycladic Blueschist Unit · Geochronology

Communicated by Dante Canil.

✉ T. A. Ducharme
  tduch009@uottawa.ca

1 Department of Earth and Environmental Science, University of Ottawa, Ottawa, Canada

2 Department of Geology, University of Vienna, Vienna, Austria

3 Instituto Andaluz de Ciencias de La Tierra (IACT), CSIC-UGR, Armilla, Granada, Spain

4 Department of Earth Sciences, University of Manitoba, Winnipeg, Canada

5 Department of Earth, Environmental and Geographic Sciences, University of British Columbia Okanagan, Kelowna, Canada

6 Department of Geology and Geoenvironment, National and Kapodistrian University of Athens, Athens, Greece

Key Points

Four sets of subvertical glaucophane-phengite-quartz veins record opening-mode brittle fracturing and syntaxial sealing

Paired $^{40}Ar/^{39}Ar$ and $^{87}Rb/^{87}Sr$ geochronology indicate Miocene crystallization, during regional greenschist facies overprint.

Fluid fO_2 above the hematite-magnetite buffer expanded the stability of glaucophane and phengite to lower P

Introduction

Hydrothermal veins are preserved throughout the rock record and appear in nearly all geological contexts. Veins are the structural record of open space created by brittle fracturing or ductile dilation, fluid infiltration, and sealing by mineral precipitation (Ramsay and Huber 1983; Bons et al. 2012). Evidence from natural examples and from numerical and analogue modelling indicates a range of opening mechanisms reflecting the tectonic framework of vein formation, and several endmember styles of crystallization during vein sealing controlled by physicochemical properties of the parental fluids (Ramsay 1980; Urai et al. 1991; Bons 2001; Bons et al. 2012). Veins accordingly represent a valuable record of stress conditions and fluid regimes coeval with their formation. These aqueous fluids may moreover act as conduits for advective mass transfer, driving metasomatic alteration that may extend to the km-scale (Bebout and Barton 1993; Harlov and Austrheim 2013). Whereas veins in the rock record are disproportionately composed of carbonate minerals or quartz, the unique chemical environment of some hydrothermal systems may produce more complex metamorphic mineral assemblages that offer insight into contemporaneous pressure and temperature (PT) conditions.

Rare examples of veins hosted within exhumed high-pressure, low-temperature (HP-LT) terranes may exhibit structural or mineralogical evidence suggesting the veins formed, or were metamorphosed at, blueschist to eclogite facies conditions (e.g., Gao and Klemd 2001; Widmer and Thompson 2001; Behr and Bürgmann 2021; Muñoz-Montecinos et al. 2020; Giuntoli and Viola 2022). High-pressure veins frequently display strain elements indicative of opening, at least partially, via brittle fracturing, despite having apparently formed below the brittle-ductile transition zone (e.g., Philippot and Selverstone 1991; Castelli

et al. 1998; Spandler and Hermann 2006; Bukała et al. 2020). Veins from these settings provide insight into the fluid compositions and hydrothermal regimes characteristic of subduction zone systems and represent candidates for a geologic record of deep-seated seismological phenomena like slow slip and non-volcanic tremor (e.g., Behr and Bürgmann 2021; Menegon and Fagereng 2021; Giuntoli and Viola 2022). Correctly interpreting structures as relating to sub-arc volatile flux or deep seismogenic processes invariably requires the deconvolution of successive metamorphic mineral assemblages and (micro)structures. Despite significant recent advancements, however, thermodynamic modelling of fluid-rock interactions in metamorphic systems remains a challenging task (e.g., Huang and Sverjensky 2019; Menzel et al. 2020), due to the largely unexplored solubility of major elements in aqueous fluids and mismatch between thermodynamically- and empirically-derived solubilities (Tiraboschi et al. 2018; Macris et al. 2020). Consequently, conclusions drawn from such systems often rely on the validity of a priori inferences of contemporaneous PT conditions using minerals in the veins or surrounding host rock.

Herein, we describe syntaxial glaucophane-phengite-quartz veins in the Cycladic Blueschist Unit (CBU) of southern Evia (NW Cyclades, Greece). We utilize a multi-analytical approach incorporating mineral chemistry, geochronology, and stable isotope thermometry to develop a conceptual model for the paragenesis of the veins. In our model, fractures preferentially formed in metabasaltic rock of a complexly folded quartzite and metabasalt of a metaophiolitic sequence. Although they contain dense selvages of glaucophane and phengite—minerals considered diagnostic of HP-LT conditions—the veins exhibit undeformed planar geometries and are oriented uniformly within their tectonized and rheologically stratified host rock package. The data collectively reveal that vein formation likely coincided with regional retrograde greenschist facies metamorphism and that the nominally HP minerals crystallized as a consequence of the local bulk composition imposed, in part, by the throughgoing fluids. We argue that the mineral assemblage in the veins developed under elevated pressures in the greenschist facies during exhumation, despite superficially resembling a blueschist facies assemblage. Our conclusions underscore recent evidence from thermodynamic models demonstrating that rock exhumed from the subduction channel may exhibit coeval, ostensibly greenschist or blueschist facies mineral assemblages dependent primarily on the bulk chemistry of a local reacting volume (e.g., Manzotti et al. 2020; Muñoz-Montecinos et al. 2020).

Cenozoic tectonics of the Cyclades

The Cycladic archipelago and parts of the Attic peninsula in the Aegean Sea are composed predominantly of the CBU, an HP-LT metamorphic nappe (Dürr et al. 1978; Jacobshagen 1986). The CBU underwent Eocene HP-LT metamorphism at *c.* 50 Ma and likely remained at HP conditions until at least the middle or late Eocene (Tomaschek et al. 2003; Schneider et al. 2011; Huet et al. 2015; Laurent et al. 2021; Uunk et al. 2022). The CBU experienced syn-orogenic wedge extrusion in the late Eocene prior to unroofing into the upper crust along a series of regional-scale, low-angle detachment faults active since the early Miocene (Tomaschek et al. 2003; Ring et al. 2007a; Jolivet et al. 2010; Grasemann et al. 2012; Laurent et al. 2017). The CBU sustained greenschist facies overprint of variable intensity during late syn-orogenic and post-orogenic exhumation (Schliestedt and Matthews 1987; Ring et al. 2010).

The southernmost region of Evia is occupied by two lithological units corresponding to the CBU: the predominantly metacarbonate Styra Unit, and the overlying, partly ophiolitic Ochi Unit, which comprises ultramafic, mafic, and felsic igneous rocks and quartzitic metasediments and ironstones (Katsikatsos et al.,1991a; Katzir et al. 2000; Xypolias et al. 2012; Fig. 1). The Ochi Unit has alternatively been correlated with the Makrotantalon Unit situated at the top of

the structural pile of Andros to the southeast (Papanikolaou 2009; Gerogiannis et al. 2019). The Ochi Unit is interpreted to have been thrust atop the Styra Unit in the subduction channel prior to the pervasive reworking of the nappes by multiple generations of folds (Xypolias et al. 2012). The CBU-affiliated units structurally overlie a ~ 3 km thick parautochthonous platform carbonate and flysch sequence that is exposed in a tectonic window in south-central Evia (Katsikatsos et al. 1991b; Shaked et al. 2000; Ducharme et al. 2022). The entire structural pile of southern Evia is situated in the footwall of the North Cycladic Detachment System (NCDS), a fault network extending from Samos across the northern Cyclades to Evia (Jolivet et al. 2010). The NCDS was likely partly responsible for post-orogenic exhumation of southern Evia, and its influence is recorded by numerous top-to-N and top-to-NE kinematic indicators preserved up to 500 m below the detachment (e.g., Mehl et al. 2007; Jolivet et al. 2010; Menant et al. 2013; Laurent et al. 2015; Ducharme et al. 2022).

The CBU-equivalent units of southern Evia experienced peak HP-LT metamorphism of ~ 10–12 kbar and ~ 400–460 °C (Shaked et al. 2000; Katzir et al. 2000; Ducharme et al. 2022). Whereas the timing of peak HP-LT metamorphism likely coincides with that of the broader CBU, relevant $^{40}Ar/^{39}Ar$ and $^{87}Rb/^{87}Sr$ geochronology from the Styra and Ochi units has yielded dates for phengitic white mica and glaucophane between *c.* 35–30 Ma (Maluski
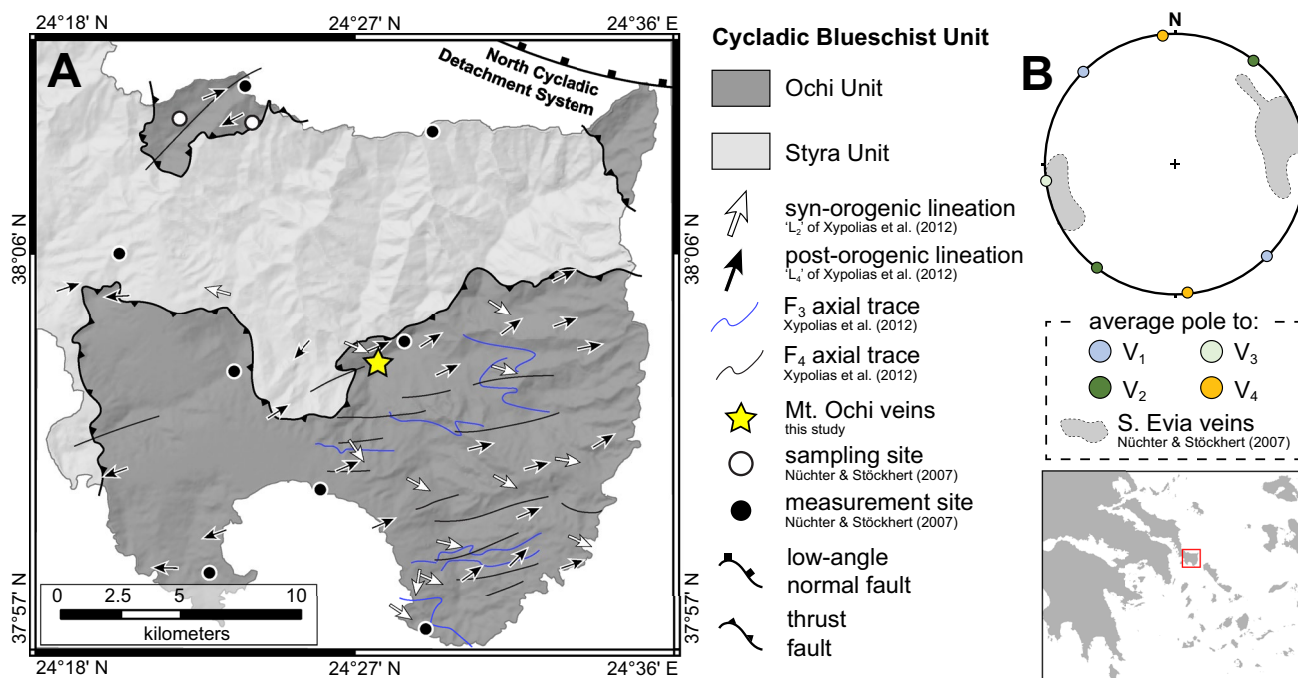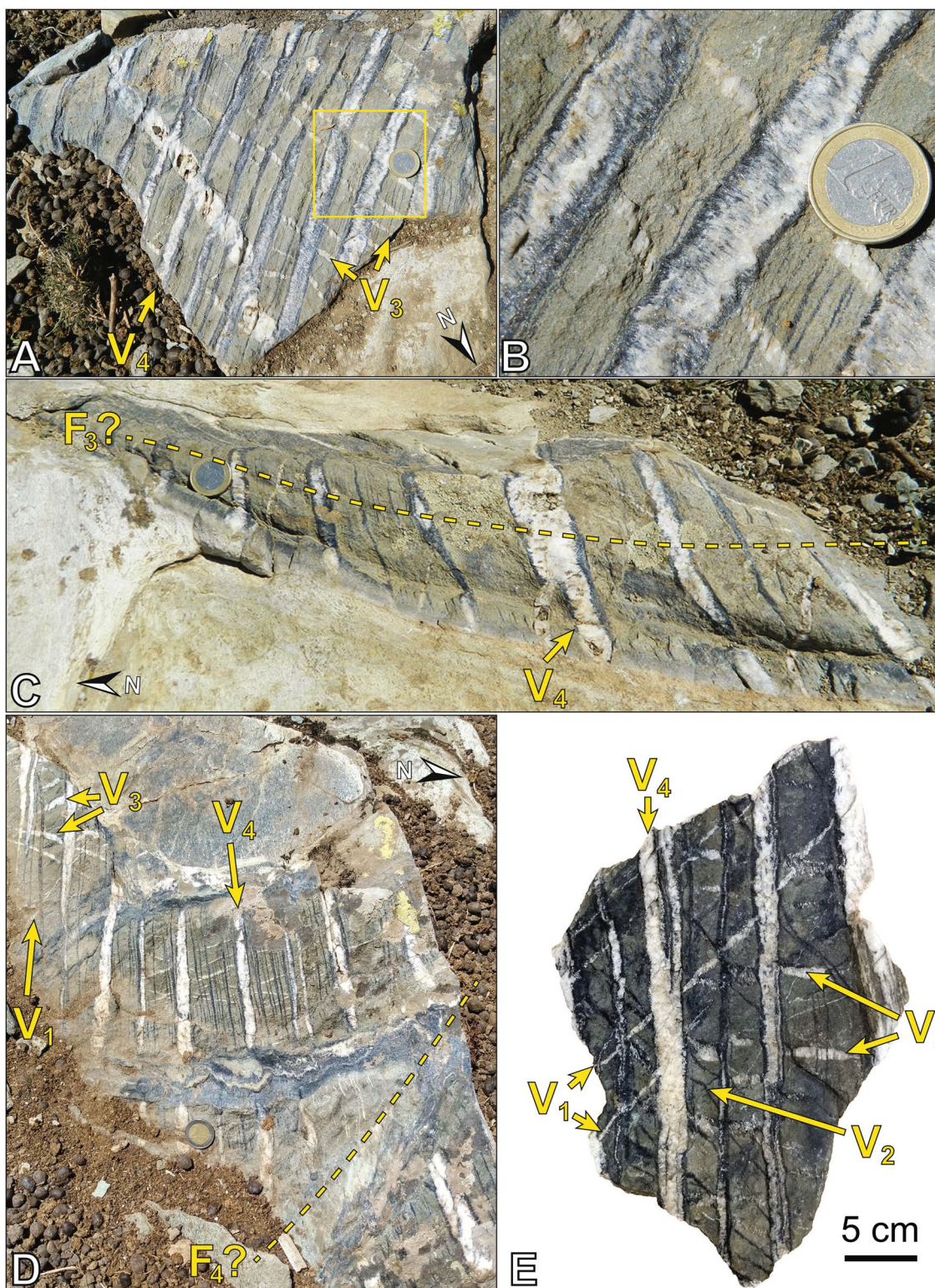

Fig. 1 A Geologic map of southern Evia. Modified after Katsikatsos et al. (1991) and Xypolias et al. (2012). **B** Stereonet showing average poles to each vein set, and includes vein measurement data (shaded region) from Nüchter and Stöckhert (2007). Inset map shows the location of the study area NW of the Cyclades

et al. 1981; Ring et al. 2007b; Ducharme et al. 2022). Similar dates obtained elsewhere in the Cyclades have been interpreted as capturing the timing of earliest greenschist or latest blueschist facies metamorphism, incipient strain related to the major detachments, or else a geologically meaningless mixture of contrasting age domains (Cossette et al. 2015; Laurent et al. 2021). Greenschist facies overprint of the CBU on Evia is considered to have begun by *c*. 25–21 Ma (Ring et al. 2007b; Ducharme et al. 2022), coeval with estimates for the remainder of the CBU to the south.

◄**Fig. 2** Outcrop photographs of the Mt. Ochi glaucophane-bearing veins. **A** Representative photo showing prominent, evenly-spaced V_4 veins hosting dense glaucophane + quartz. The prominent veins cross-cut and offset numerous V_3 veins of varying widths containing mostly quartz. Box shows location of figure B. **B** Close-up photo showing the distribution of glaucophane within the V_4 veins and the cross-cutting relationship of V_3 veins by narrow glaucophane-rich seams. **C** V_4 veins of variable width transecting an upright folded (F_3) metabasalt horizon. The metabasalt is overlain on either side by quartzite with a mineral lineation defined by glaucophane. **D** Evenly-spaced V_4 veins cross-cutting smaller V_1 and V_3 veins. A tight flat-lying fold (F_4?) outlined by glaucophane crystals appears to cross-cut the V_4 veins, but veins reappear apparently undisturbed on the opposite side. **E** Sample EV19-15C indicating the structures used to define the vein set nomenclature. Fold nomenclature after Xypolias et al. (2012)

Vein mineralogy and structure

Distinct vein sets containing sodic amphibole (optically identified as predominantly glaucophane) + quartz ± white mica ± epidote locally occur in an exposure of the Ochi Unit directly west of Mt. Ochi (UTM Zone 35N, E277323, N4215232.; Figs. 1, 2a). The most prominent vein set cross-cuts all others and contains dense selvages of glaucophane oriented at high angles to the vein walls (Fig. 2b). The veins are hosted within medium-grained metabasites and schistose quartzite tectonically intercalated at the cm-scale, but preferentially within the metabasic layers, pinching out or terminating abruptly near contacts between the two lithotypes. In plan view normal to the metamorphic layering, the coarser-grained metabasites are dissected by four differently oriented vein sets, each of which contains variable modal proportions of the three main constituent minerals. Despite evidence of folding in the host rocks, veins retain a dominantly planar geometry (Fig. 2c–d).

The metabasic lithology is orange-brown to green–brown in color and exhibits a granular appearance, lacking macroscopically identifiable minerals apart from a dominant prismatic phase locally defining an ENE-WSW trending mineral lineation. Intercalated quartzites are a pale buff or cream color with abundant blue prismatic glaucophane crystals, up to 3 mm long, distributed throughout a fine-grained matrix. The glaucophane defines a weak mineral lineation oriented at a small angle to the lineation in the metabasites, and subparallel to the most prominent vein set. Thin (~ 1 mm) seams of almost exclusively glaucophane are parallel to this vein set, apparently concentrated along contacts between the two dominant host lithologies.

Four samples (EV19-15A, B, C, D; Table 1) of the veined rocks were collected for laboratory investigation; additional micrograph documentation is provided in the supplementary information file (Figs. S1, S2). Petrographic study reveals that the metabasites are composed mostly of moderately (2nd order) birefringent, elongate prismatic clinopyroxene

(70–75%) and interstitial anhedral albite (10–15%; Fig. 3a). Euhedral aggregates of albite are the dominant phase in several thin layers where partial relicts of prismatic clinopyroxene occur as inclusions. Other minerals include euhedral crystals of glaucophane, phengite, and epidote, the latter of which forms abundant euhedral inclusions in albite. Chlorite is locally predominant over albite and occupies the interstices of clinopyroxene grains, and appears as a major phase alongside glaucophane and minor biotite in some albite-dominated layers (Fig. 3b).

Clinopyroxene is preserved in various states of alteration. In places, clinopyroxene crystals retain a clear prismatic morphology and individual crystals may still be discerned in transmitted light. Backscatter electron imaging in these regions nevertheless reveals that clinopyroxene is occluded by dense subrounded quartz inclusions < 10 μm in diameter (Fig. 4a). Quartz inclusions are seldom distinguishable in transmitted light. Where quartz is visible in transmitted light, it occurs alongside euhedral crystals of glaucophane, phengite, and epidote, and clinopyroxene takes on a fuzzy appearance due to skeletal intergrowth with either quartz (Fig. 4b) or albite (Fig. 4c).

The schistose quartzite comprises aggregates of quartz (60–70%) with dispersed white mica (15%), glaucophane (15%), hematite, and minor albite (Fig. 3c). Quartz forms fine-grained granoblastic recrystallized aggregates with grain dimensions limited by the surrounding fine-grained phyllosilicates. Preferred orientations of the long axes of glaucophane and white mica, as well as a subtle shape preferred orientation (SPO) of quartz, collectively define a planar foliation.

Each vein set hosts variable proportions of sodic amphibole + quartz ± white mica ± epidote. Glaucophane displays a conspicuous compositional zonation in nearly all occurrences (Fig. 5a); mica, in contrast, is not zoned (Fig. 5b). Quartz, epidote, and infrequent titanite are common inclusions in glaucophane cores (Fig. 5c). Glaucophane and phengite form large,

pristine crystals displaying elongate prismatic or tabular habits. Both minerals are found primarily in systematic orientations along vein walls but also occur sparsely in the vein cores. Host rock fragments are commonly included within veins, most often as elongate wall-parallel inclusions (Fig. 5d). Hereafter we briefly describe each vein set that we have discriminated the nomenclature for which was developed using a sample (EV19-15C) containing most of the vein sets observed across the exposure (Fig. 2e).

V_1 veins. The oldest vein population (V_1) strikes NE-SSW, and are commonly < 5 mm wide with parallel walls and a planar geometry. Quartz is the predominant constituent of V_1 veins, the margins of which are lined with dispersed, dense clusters of phengite and glaucophane,

Table 1 Summary of samples of the Mt. Ochi veins

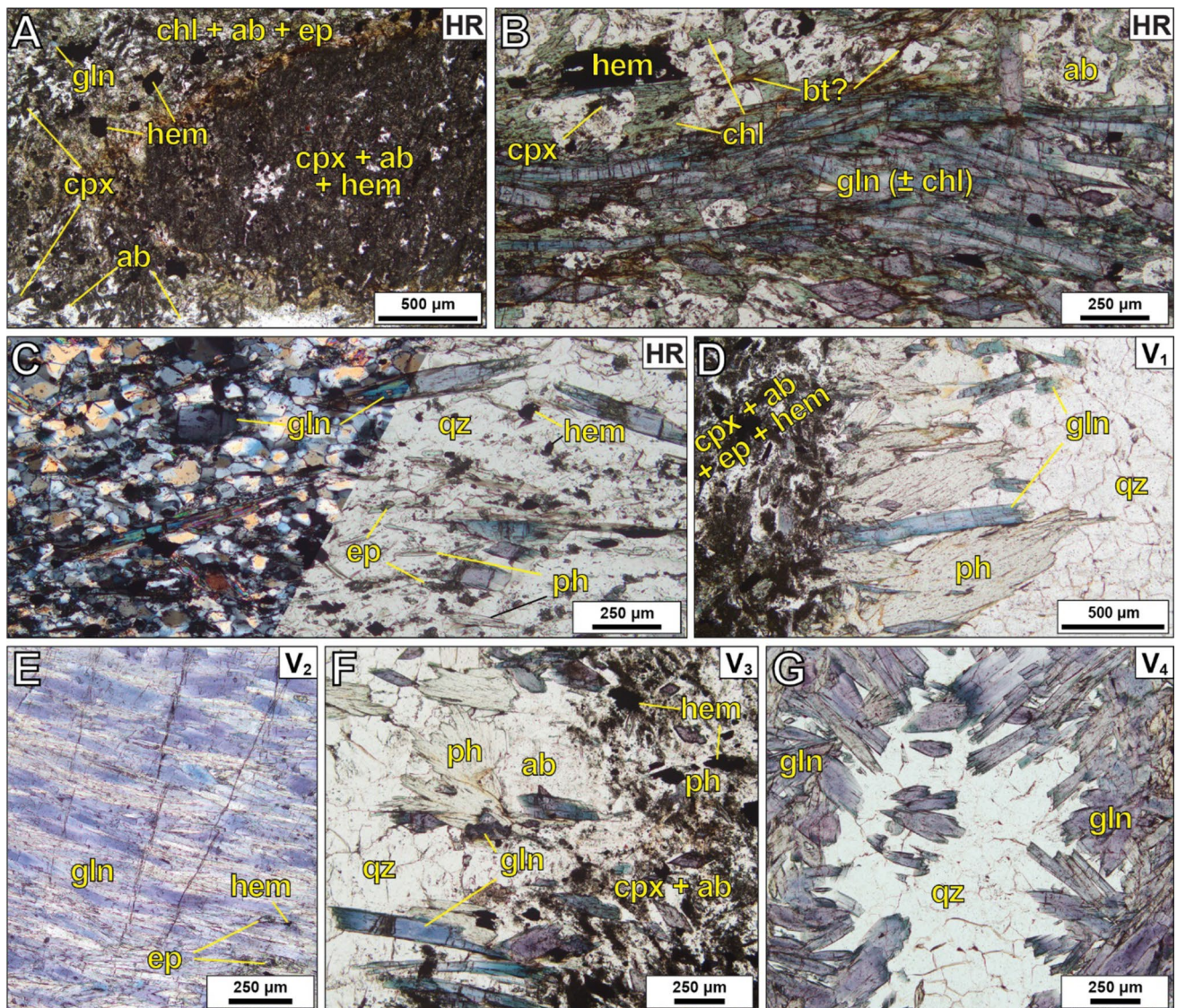| Sample ID	Vein sets	Host rock contacts	$^{87}Rb/^{87}Sr$	$^{40}Ar/^{39}Ar$	^{18}O
EV19-15A	V_3, V_4	planar			
EV19-15B	V_3, V_4	undulose, isoclinally folded			
EV19-15C	V_1, V_2, V_3, V_4	planar	x	x	x
EV19-15D	V_2, V_3, V_4	isoclinally folded	x	x	

Fig. 3 Micrographs of major vein sets and their host rocks (HR). **A** Fragment of minimally altered metabasaltic host rock surrounded by a more typical albite + epidote + clinopyroxene + chlorite assemblage. (Plane-polarized light; PPL). **B** Seam of glaucophane intergrown with chlorite in an albite-dominated host rock layer (PPL). **C** Typical schistose quartzitic host rock layer. Micrograph divided into cross-polarized light (XPL, left) and PPL (right) to illustrate the crystalline structure of quartz. **D** Margin of a V_1 vein showing inward growth of phengite and glaucophane from the metabasaltic wall rock. YZ plane of the vein is shown (PPL). **E** Interlocking glaucophane crystals from a V_2 vein. Note the alternation between pleochroic extremes (colorless to violet). YZ plane of the vein is shown (PPL). **F** Margin of a V_3 vein showing wall rock at the margin that has undergone significant alteration to albite. YZ plane of the vein is shown (PPL). **G** Centre of a V_4 vein shows a seam of quartz transecting glaucophane oriented at a high angle to the vein walls (parallel to the vertical of the photo). XY plane of the vein is shown (PPL). *ab* albite, *bt* biotite; *chl* chlorite; *cpx* clinopyroxene; *ep* epidote; *hem* hematite; *ph* phengite; *qtz* quartz
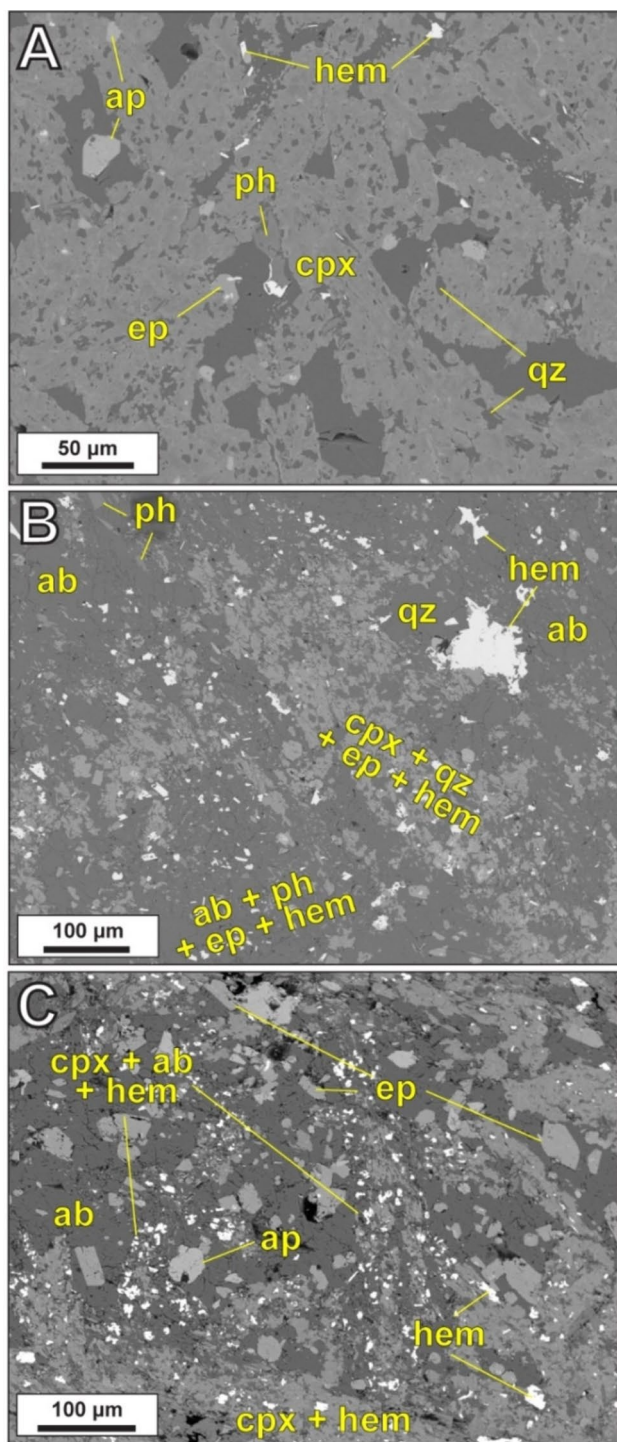
Fig. 4 Backscatter electron images of host rock clinopyroxene in various stages of alteration. **A** Poikiloblastic clinopyroxene envelops numerous inclusions of quartz. **B** Skeletal clinopyroxene exhibiting partial replacement by quartz and hematite. **C** Skeletal clinopyroxene exhibiting comprehensive replacement by albite and hematite. *ab* albite, *ap* apatite, *cpx* clinopyroxene, *ep* epidote, *hem* hematite, *ph* phengite, *qtz* quartz

with phengite generally present in greater size and abundance (Fig. 3d). The long axes of these minerals are either sub-perpendicular or else at an angle of ~40–50°, to the vein walls. Quartz shows a well-developed SPO parallel to the inclined mica and amphibole, except in some vein cores, where large grains exhibit only undulatory extinction (Fig. 5e). Quartz grain boundaries are ubiquitously serrated and exhibit low-amplitude bulging with dispersed small grains distributed along grain boundaries.

V_2 *veins.* V_2 veins strike NW–SE, are few in number, and composed almost entirely of interlocking glaucophane crystals with some vein cores of mica, minimal quartz, and rare epidote. Glaucophane crystals line the walls of V_2 veins at an oblique angle to the vein walls with a moderately distorted prismatic morphology. Mutually impinging glaucophane crystals in these veins display regular alternation between two nearly orthogonal crystallographic orientations (Fig. 3e).

V_3 *veins.* This vein generation strikes NNW-SSE (Fig. 2a) or locally defines a conjugate set with small angles at ~30° from this trend (Fig. 2d). V_3 veins frequently exhibit a lenticular shape with the highest aperture ratios of all veins studied. The prevalence of nominal HP minerals in V_3 veins is variable, ranging from quartz-dominated veins with few phengite and glaucophane crystals, to comprising almost exclusively the latter two minerals. Phengite and glaucophane are oriented at moderate or high angles to the vein walls (Fig. 3f) and are often colinear with another nominal HP mineral grain on the opposing vein wall. Quartz defines a well-developed SPO parallel to the long axes of glaucophane and phengite with predominantly lobate to serrated grain boundaries.

V_4 *veins.* The youngest, largest and most consistently developed vein set, V_4 veins are planar, spaced at regular intervals of 5–10 cm, and strike consistently ENE-WSW (Fig. 1b). Veins are up to 30 mm in width, with dense selvages of glaucophane oriented at high angles to the vein walls with a central quartz seam (Fig. 3g). Approximately 30–40% of V_4 veins within a given rock volume are < 1 mm wide and are dominated by elongate single glaucophane crystals spanning the full width of the fractures, with only minor interstitial quartz (Fig. 5c). Cores of V_4 veins and vertical extensions toward bounding ductilely deformed layers are conversely composed of quartz with dispersed euhedral glaucophane and phengite. Quartz in V_4 veins locally exhibits low-amplitude grain boundary bulging and serrated boundaries, but notably less pervasively than in other veins.

Solid inclusion trails comprising small amphibole crystals are a common feature of V_4 veins (Fig. 5d). In intermediate-width veins, inclusion trails may span from one
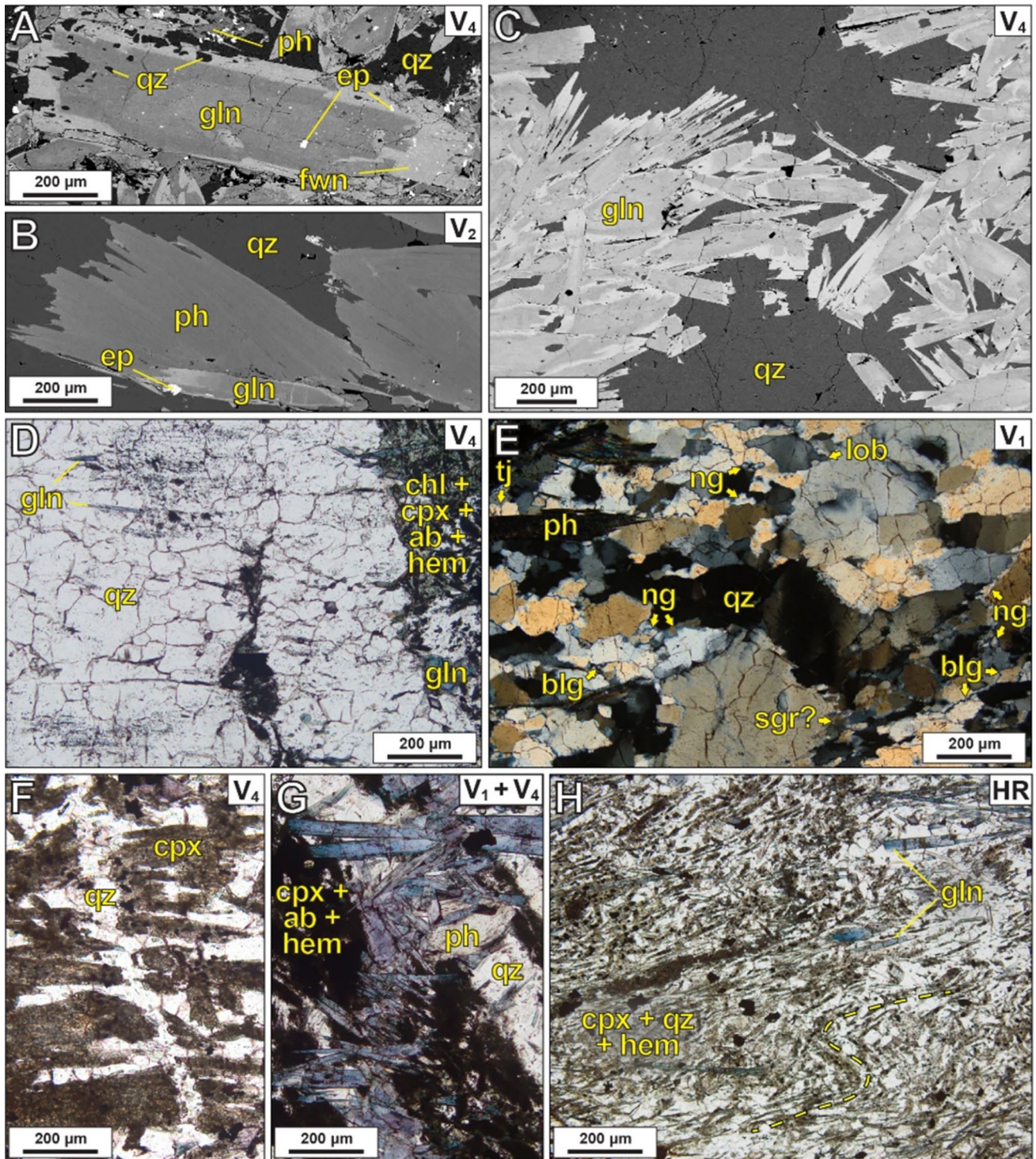
glaucophane-rich selvage to the other. Toward the vein core, these features are isolated within one or more quartz grains. Some narrow fractures parallel to V_4 are predominantly filled either by quartz or glaucophane. The former veins show puzzle-like geometry of transected clinopyroxene grains, suggesting the sealing of transgranular fractures (Fig. 5f). In the latter, glaucophane crystals span the full width of the fractures (Fig. 5g).

Other structures. Several additional structures occur either too infrequently or too isolated from larger structures to place within the relative age hierarchy of the more abundant vein sets. Numerous small curvilinear veinlets

◄Fig. 5 Micrographs and electron backscatter images of structural and mineralogical features of the Mt. Ochi veins. **A** Backscatter electron image of a large glaucophane grain exhibiting typical core-to-rim zoning. **B** Backscatter electron image of a phengite grain showing relative compositional homogeneity. **C** Photomicrograph of an XY (foliation-parallel) section of a V_4 vein. Note the common inclusions of quartz in glaucophane cores. **D** Photomicrograph from a V_4 vein showing mineral inclusion trails in the vein quartz and a solid inclusion band of entrained host rock. YZ plane of the vein is shown (PPL). **E** Core of a V_1 vein showing typical vein quartz textures. Elongate quartz grains with interlobate and bulging grain boundaries at the margins of the micrograph are truncated by large quartz crystals showing undulatory extinction and incipient subgrain development. XY plane of the vein is shown (XPL). **F** Narrow quartz vein infilling a transgranular fracture which cross-cut clinopyroxene grains in metabasaltic host rock. YZ plane shown (PPL). **G** Narrow V_3 vein sealed by elongate glaucophane spanning the width of the fracture. XY plane shown (PPL). **H** Shear zone within a quartz-flooded section of a host metabasalt. Elongate clinopyroxene crystals trace the outline of tight folds with sub-horizontal axial planes (PPL). Mineral abbreviations: *ab* albite, *chl* chlorite, *cpx* clinopyroxene, *ep* epidote, *fwin* ferriwinchite, *hem* hematite, *ph* phengite, *qtz* quartz. Microstructure abbreviations: *blg* grain boundary bulging, *lob* lobate grain boundary, *ng* new recrystallized grain, *sgr* subgrain rotation recrystallization, *tj* grain boundary triple junction

filled with glaucophane + quartz occur in an orientation subparallel or slightly oblique to V_4 veins, but these are typically isolated from other structures within intact host rock. One thin (> 0.5 mm) foliation-parallel seam comprising coarse epidote + glaucophane + hematite (sample EV19-15D) cross-cuts all earlier structures but is transected by a later (V_4?) vein generation. Several small sub-horizontal shear zones are developed within both the metabasic and schistose layers, where the prismatic ferromagnesian mineral aggregates outline kinks or tight folds, but individual crystals retain largely intact euhedral crystal shapes (Fig. 5h). These shear zones are cross-cut by V_4 veins, with no evidence of phengite or quartz within the transecting vein material having accommodated greater shear relative to other parts of the vein.

Analytical Methods

Scanning electron microscopy and electron microprobe analysis

Four standard 30 μm thick polished sections (one from EV19-15A and three from EV19-15C) were selected for analysis as these samples permitted straightforward discrimination between vein sets. Cores, mantles, and rims of white mica and amphibole specimens were analyzed using a 10 μm diameter spot size to determine any compositional zoning. Preliminary reconnaissance and mineral identification on the scanning electron microscope (SEM) by electron dispersive spectroscopy (EDS) was performed at the University of Ottawa (Ottawa, Canada)

using a JEOL 6610LV SEM. Quantitative wavelength-dispersive spectroscopy (WDS) microprobe analyses were conducted at the University of Ottawa using a JEOL JXA-8230 SuperProbe. Full analytical details can be found in the data repository.

In-situ $^{87}Rb/^{87}Sr$ geochronology

Three 100 μm thick polished sections were prepared from samples EV19-15C and EV19-15D for *in-situ* $^{87}Rb/^{87}Sr$ geochronology using an Agilent 8900 triple-quadrupole inductively coupled plasma mass spectrometer equipped with a reaction cell (Zack and Hogmalm 2016; Hogmalm et al. 2017) paired to an ESL 193 Excimer laser with a Two-Vol3 ablation cell in the Fipke Laboratory for Trace Element Research at University of British Columbia, Okanagan (Kelowna, Canada). The analyses followed the basic procedures outlined in Larson et al. (2023) with both phengite and sodic amphibole ablated using a 50 μm diameter spot, a repetition rate of 10 Hz and a laser fluence of 4 J/cm^2. Analyses of secondary reference materials, including the in-house white mica MA1 (*c.* 350 Ma, A. Camacho, unpubl. data) and the nano-powdered biotite Mica-Fe (310 ± 10 Ma, Govindaraju 1979; 305.4 ± 2.0 Ma, Rösel and Zack 2022), yielded dates that overlap within error of those expected (347 ± 3 Ma and 306 ± 3 Ma, respectively). Isochron calculations excluded analyses with high uncertainty, using a > 30% (2 standard error of the mean) cut-off that resulted in the exclusion of twelve glaucophane analyses from EV19-15D and zero phengite analyses. Data processing and visualization were performed using the online version of the IsoPlotR package (Vermeesch 2018).

$^{40}Ar/^{39}Ar$ geochronology

Material belonging to V_3 and V_4 veins and the schistose quartzite host rock from EV19-15C and EV19-15D was isolated with a finishing saw and lightly crushed in a mortar and pestle. The crushed material was then sieved to obtain the 256–512 μm and 128–256 μm size fractions, from which 50–60 grains of both white mica and glaucophane were hand-picked for $^{40}Ar/^{39}Ar$ geochronology. $^{40}Ar/^{39}Ar$ analytical work was performed at the University of Manitoba (Winnipeg, Canada) using a multi-collector Thermo Fisher Scientific ARGUS VI mass spectrometer, linked to a stainless steel Thermo Fisher Scientific extraction/purification line and Photon Machines (55 W) Fusions 10.6 CO$_2$ laser. Full analytical details can be found in the data repository.

Oxygen isotopes

Vein material belonging to V_1, V_3, and V_4 veins from EV19-15C was isolated with a finishing saw and lightly crushed in
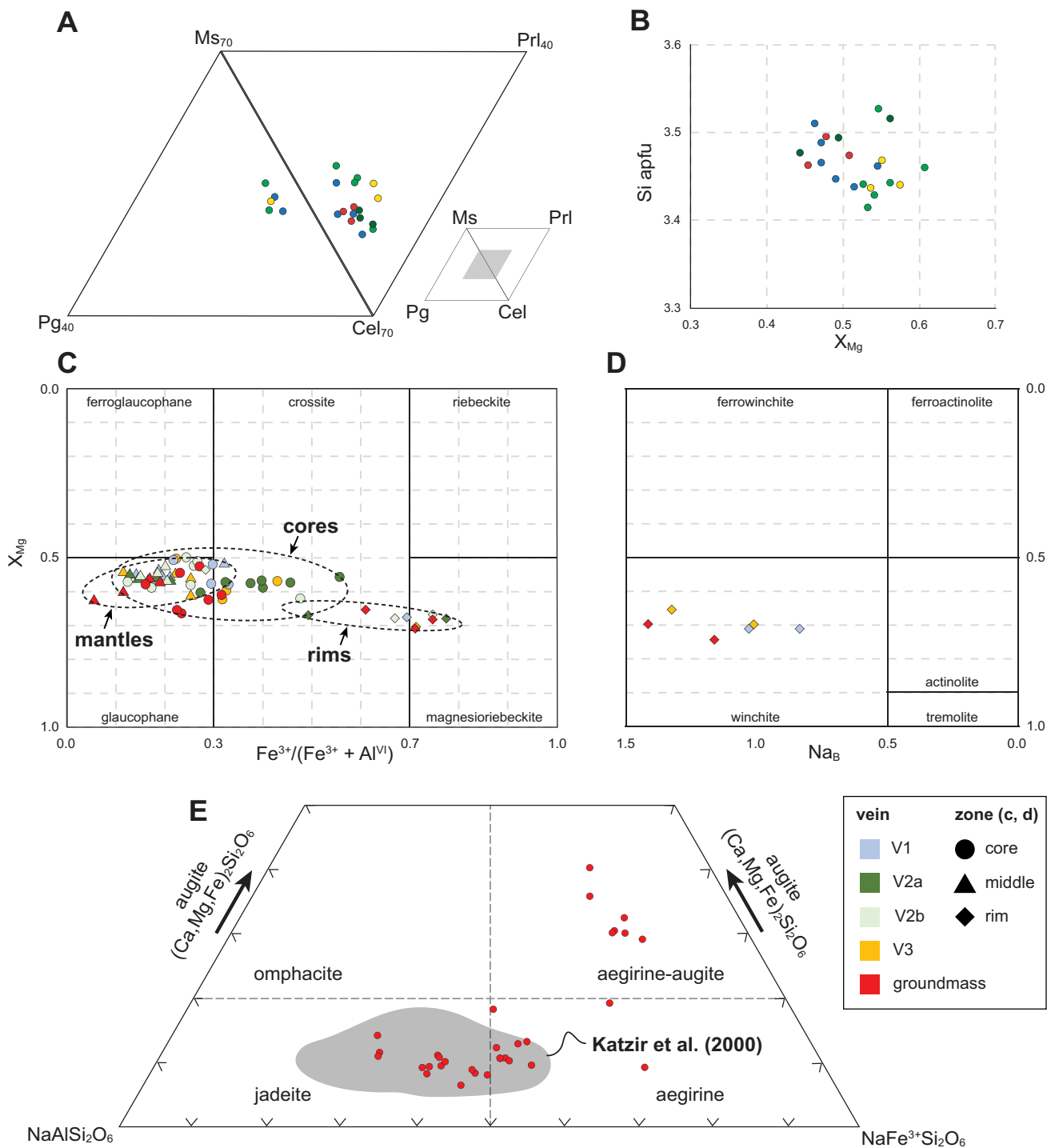
Fig. 6 Mineral chemistry plots for HP minerals in the Mt. Ochi veins and their host lithotypes. **A** Abbreviated dual mica ternary diagrams. **B** White mica Si apfu vs X_{Mg} plot. **C** Sodic and **D** sodic-calcic amphibole X_{Mg} vs $Fe^{3+}/(Fe^{3+} + Al)$ plot after Hawthorne et al. (2012). **E** Abbreviated pyroxene jadeite-aegirine-augite ternary plot. Shaded region summarizes data from Katzir et al. (2000)

a mortar and pestle. The crushed material was then sieved to obtain the 256–512 μm and 128–256 μm size fractions, from which 15–20 mg each of inclusion-free quartz and mica was hand-picked. The material was analyzed at the Queens Facility for Isotope Research at Queens University (Kingston,

Canada) via boron pentafluoride digestion using a Thermo Scientific MAT 253 stable isotope ratio mass spectrometer. Analytical errors are 0.4‰ and are reported relative to Vienna Standard Mean Ocean Water (VSMOW).

Mineral chemistry

Electron microprobe (EMP) analyses were used to define white mica and amphibole chemistry and investigate compositional variations across and within the vein sets. Full data tables can be found in Table S1. White mica compositions from all veins and the host rock plot in a restricted range between muscovite and celadonite (i.e., phengite) with elevated Si content (Si apfu: 3.43–3.53, mean: 3.46; Fig. 6a) and uniform intermediate X_{Mg} (0.45–0.61; Fig. 6b). Variations were neither observed from core to rim within single crystals, nor among populations occupying different vein sets, although biotite present along cleavage planes affected some excluded EMP analyses. Pyrophyllite and paragonite consistently comprise < 0.05 mol fraction of each analysis.

Amphibole recalculations were performed using the formula of Locock (2014), and hereafter we employ the nomenclature of Hawthorne et al. (2012). Amphibole displays concentric zonation visible in transmitted light and backscatter images (Fig. 5a). Cores and mantles are glaucophane, with compositions slightly below the glaucophane-ferroglaucophane divide (X_{Mg}: ~0.5; Fig. 6c). Mantles are comparatively Al enriched relative to the cores. The outermost rims appear bright in backscatter images and display a deep green–blue pleochroism in transmitted light. Rim Ca contents commonly exceed 0.5 apfu and exhibit wider compositional variability, ranging from glaucophane to magnesiorebeckite to (ferri-)winchite (Fig. 6c-d). Similar to white mica, sodic amphibole compositions display no resolvable systematic variation across both the vein sets and host rock, including in their core-to-rim chemistry. In addition to the large, zoned specimens of sodic amphibole, several isolated and unzoned euhedral crystals were observed in the ductily deformed groundmass as well as in V_3 veins. Analysis of these isolated grains by EDS indicates these are either ferriwinchite or, less frequently, actinolite.

Microprobe analyses were also conducted on host rock feldspar, clinopyroxene, epidote, and chlorite. Feldspar is consistently endmember albite (An_{0-2}) regardless of host lithology. Epidote and chlorite are relatively invariant in composition. Epidote group phases exhibit $Fe^{3+}/(Fe^{3+} + Al) = 0.28–0.32$, classified as epidote following the nomenclature of Armbruster et al. (2006). Chlorite is close to ideal clinochlore and generally exhibits full octahedral site occupancy, with $X_{Fe} = 0.45–0.52$.

Notably, clinopyroxene compositions varied across samples. Clinopyroxene formulae were recalculated following Cawthorne and Collerson (1974), with Fe^{3+} (i.e., aegirine) assumed to be in equal molar abundance to molar Na in excess of Al (i.e., jadeite). In EV19-15A and EV19-15B, clinopyroxene defines a wide array spanning the jadeite-aegirine join, from $Jd_{60}Aeg_{30}Di_{10}$ at the jadeite-rich extreme

and up to $Jd_{40}Aeg_{50}Di_{10}$ at the aegirine-rich extreme, consistent with earlier data from Ochi metabasalt (Katzir et al. 2000). A segment of the host rock relatively poor in glaucophane and white mica locally displayed irregular but distinguishable cores and rims within prismatic clinopyroxene grains. Cores here were among the most jadeite-rich specimens measured, whereas rims showed a marked increase in aegirine component. Clinopyroxene from sample EV19-15C exhibited comparatively high Ca and low Al, plotting as aegirine-augite with average composition $Jd_{19}Aeg_{53}Di_{29}$.
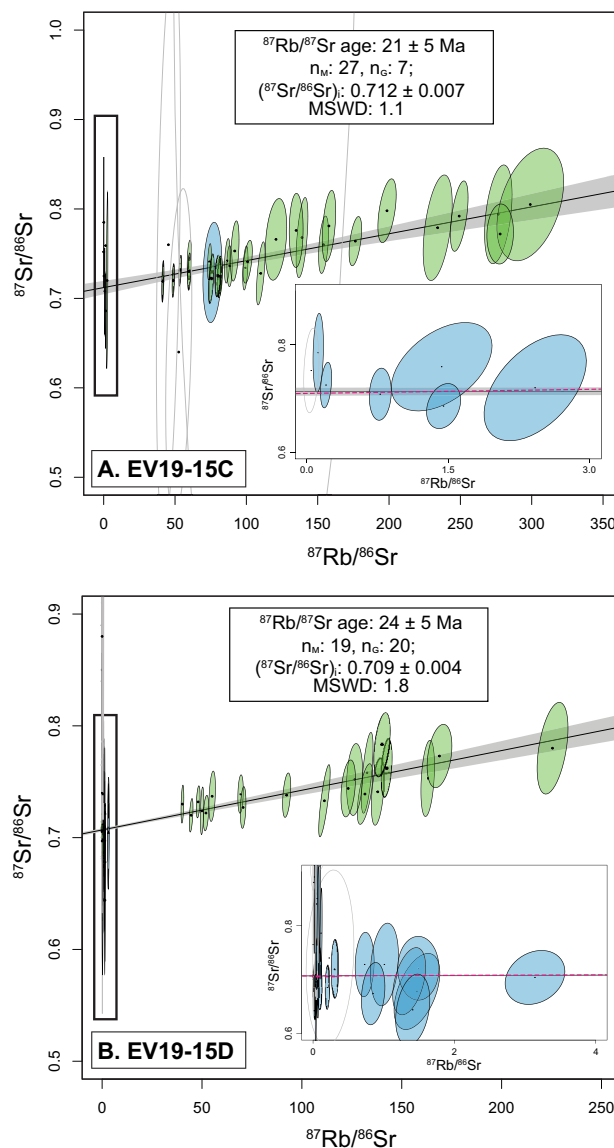

Fig. 7 Isochron diagrams for *in-situ* $^{87}Rb/^{87}Sr$ analyses of glaucophane (blue ellipses) and phengite (green ellipses) hosted in the Mt. Ochi veins for **A** EV19-15C and **B** EV19-15D. Inset plot shows details of the glaucophane analyses, which cluster near the $^{87}Sr/^{86}Sr$ (low-Rb) axis. Magenta dashed line corresponds to an isochron calculated using only phengite data, showing minimal deviation from the complete two-mineral isochron. Ellipses are 2σ

In-situ $^{87}Rb/^{87}Sr$ geochronology

Phengite and glaucophane were dated in situ from specimens hosted in V_1-V_4 in EV19-15C, and V_2-V_4 in EV19-15D. Phengite analyses define a linear array, forming a low-dispersion isochron. Glaucophane analyses were comparatively Rb-poor and accordingly the data clusters near the $^{87}Sr/^{86}Sr$ (Y-) axis. Analyses of glaucophane display a high degree of scatter about the Y-axis consistent with low Sr concentrations (Table S2). The higher precision glaucophane analyses, however, plot along the same isochron as the phengite. A single glaucophane analysis from EV19-15C yielded an $^{87}Rb/^{86}Sr$ ratio > 50 (Fig. 7a). Discrete chemical zones in glaucophane were narrower than the diameter of the laser ablation pit and thus could not be targeted. Accordingly, glaucophane data represent an analysis of material from the cores and mantles.

Two isochrons constructed using *in-situ* phengite and glaucophane $^{87}Rb/^{87}Sr$ spot analyses from EV19-15C and EV19-15D define mutually indistinguishable isochron ages of 21 ± 5 Ma (n_{wm}: 27, n_{gln}: 7; MSWD: 1.1) and 24 ± 5 Ma (n_{wm}: 19, n_{gln}: 20; MSWD: 1.8), respectively (Fig. 7). Each

sample produced mutually indistinguishable $(^{87}Sr/^{86}Sr)_I$ intercepts of 0.712 ± 0.007 and 0.709 ± 0.004, respectively.

$^{40}Ar/^{39}Ar$ geochronology

We also performed multiple single-grain, total-fusion $^{40}Ar/^{39}Ar$ geochronology on phengite and glaucophane from the youngest two vein sets (V_3, V_4), which were selected due to the abundance of the target phases within them. Seven to eight pristine white mica crystals (n: 22) analyzed from one V_3 vein in sample EV19-15C, and from two V_4 veins – one each from sample EV19-15C and EV19-15D – yielded total-fusion $^{40}Ar/^{39}Ar$ dates between 21.4 ± 0.6 and 23.0 ± 0.7 Ma (weighted mean: 22.2 Ma ± 0.3 Ma; MSWD: 0.62; Fig. 8; Table S3). One step-heating experiment yielded a plateau age of 22.6 ± 0.2 Ma (MSWD: 1.49; Fig. S3a; Table S3).

Vein-hosted glaucophane included both elongate prismatic single crystals and radial polycrystalline aggregates. Most specimens were opaque to weakly translucent, making it difficult to select against the presence of inclusions. Ductilely deformed groundmass from sample EV19-15D yielded mostly single translucent crystals, smaller than those obtained from the veins. Glaucophane yielded comparatively dispersed results relative to phengite, as well as numerous systematically implausible analyses. High Ca/K values (> 5) and routinely low $^{40}Ar^*$ yields produced high analytical uncertainties for most total fusion dates. Grains deemed to return acceptable or only moderately disturbed analytical results provide $^{40}Ar/^{39}Ar$ dates between 18 and 39 Ma, which together provide a weighted mean age of 26 ± 3 Ma (MSWD: 14). These grains commonly exhibit Ca/K < 5, which coupled with mineral chemical data (Fig. 6) indicate a minimal contribution from sodic-calcic rims to the analyses. A single step-heating experiment on V_4 glaucophane yielded a disturbed saddle-shaped spectrum with apparent age steps between *c.* 25 Ma and 0 Ma and an integrated age of 15.2 ± 1 Ma (Figure S3b; Table S3). Due to these analytical challenges, we emphasize the phengite data as the most reliable measure of the $^{40}Ar/^{39}Ar$ systematics in the veins.

Stable isotopes

To determine the temperature of vein formation, we conducted ^{18}O isotopic analyses of vein-hosted white mica and quartz. Quartz from V_1, V_3, and V_4 veins yielded $\delta^{18}O$ values of 14.9‰, 18.5‰, and 15.9‰, respectively, whereas phengite from the same veins yielded $\delta^{18}O$ of 10.7‰, 11.9‰, and 11.5‰. Quartz-phengite pairs provided $\Delta^{18}O$ values of 4.2‰, 6.6‰, and 4.4‰. Calculations using the quartz-phengite isotope fractionation calibration of Zheng (1993) indicate equilibration temperatures of 334 °C for V_1

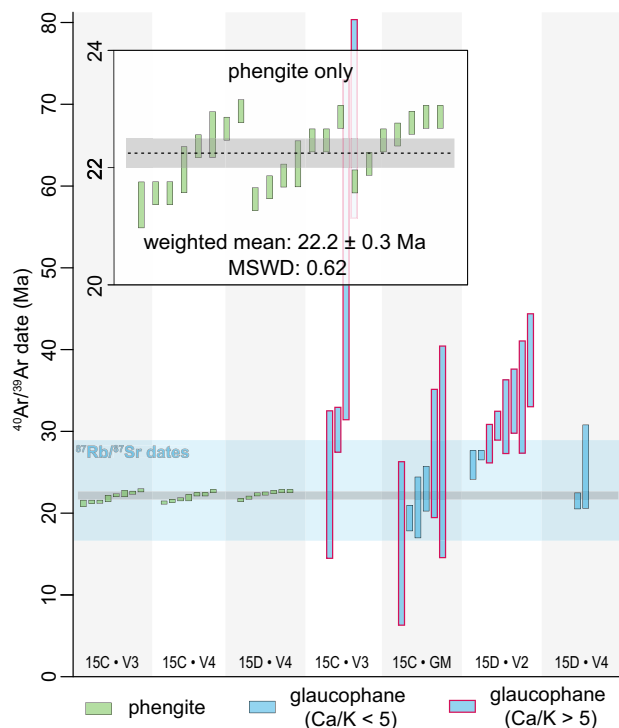**Fig. 8** Summary of new multiple, single-grain total fusion $^{40}Ar/^{39}Ar$ data for phengite (green bars) and glaucophane (blue bars) from different vein sets and the groundmass (GM) of the Mt. Ochi veins. Black line and grey error bar indicate the weighted mean age calculated using the phengite data (see text for discussion). Range of calculated $^{87}Rb/^{87}Sr$ isochron dates is indicated by the blue field. Errors are 1σ

Table 2 Summary of oxygen isotope data from the Mt. Ochi veins

Sample	Quartz (‰)[a]	2σ	Phengite (‰)[a]	2σ	Δqz-phg (‰)[a]	T_{qz-phg} (°C)[b]	±	Fluid (‰)[c]
V1	14.9	0.4	10.7	0.4	4.2	335	40	10.3
V3	18.5	0.4	11.9	0.4	6.6	172	40	5
V4	15.9	0.4	11.5	0.4	4.4	315	40	9.6

[a]Values reported relative to Vienna Standard Mean Ocean Water (VSMOW)

[b]Calculations performed using the quartz-phengite calibration of Zheng (1993)

[c]Calculations performed using the quartz-water calibration of Matsuhisa et al. (1979)

veins, 172 °C for V_3 veins, and 315 °C for V_4 veins, with 2σ errors of ± 40 °C (Table 2).

Discussion

Data outlined in the preceding sections attest to broad similarities among the mineralogical, geochronological, and (micro-)structural features of the Mt. Ochi veins, independent of their apparent relative ages. The contrasting fracture orientations nevertheless require that different vein generations formed under an apparently transient local stress field. Consequently, whereas we did not observe mutually cross-cutting relationships among the Mt. Ochi vein sets, we assume that each vein set formed over a single continuous interval, prior to the development of any successive fracture set(s). This suggests that fracture sets crossed a critical volume threshold upon which brittle failure exploiting the pre-existing fracture planes became unfavorable. Our second assumption is that sealing in all fractures was facilitated by an aqueous fluid whose composition and PT conditions favored the precipitation of a consistent mineral assemblage, albeit with variable modal proportions. This indicates that veins formed over a restricted interval during which a fluid exhibiting relatively invariant chemistry readily infiltrated newly-formed fractures at reasonably constant PT conditions, a proposal underscored further by our geochronologic data. In the following discussion, we regard the Mt. Ochi veins as essentially monogenetic features and explore the implications of this hypothesis for their paragenesis.

Fracturing and sealing mechanisms

Structural evidence from a range of scales supports the Mt. Ochi veins as having formed as opening-mode fractures. Most vein sets exhibit parallel planar walls with lenticular cross-sections and correlative features indicating opening by lateral translation of the vein walls (Figs. 2a–b, Fig. 5f). Inclusion trails within the veins (Fig. 5d) track at least part of the opening history as having proceeded at a high angle to the vein walls (Bons et al. 2012). An exception may be highlighted for V_3 veins, which display lenticular morphologies and excessively high aperture ratios (Vermilye and Scholz 1995), but whose wall geometries nevertheless favor a tensile opening mechanism.

The systematic orientation of elongate vein-hosted minerals at high angles to the vein walls indicates a syntaxial sealing mechanism, with crystal growth proceeding inward from the wall rock (Bons et al. 2012). Glaucophane and phengite exhibit well-developed crystal facets and euhdral morphologies, with phengite occasionally growing radially from the host rock, features consistent with crystallization into an open fracture (Fig. 3f). In wider veins, wall-parallel host rock inclusion trails and discontinuous mineral inclusion bands have been identified (Fig. 5d), microstructures that are commonly associated with crack-seal veins (Ramsay et al. 1980; Uysal et al. 2011; Bons et al. 2012). However, the Mt. Ochi veins show no direct microstructural evidence for incremental brittle failure and sealing. On the contrary, solid inclusion trails are generally isolated occurrences, and, moreover, the concentric zonation of glaucophane implies an uninterrupted interval of growth. Wall-parallel fluid inclusion trails are likewise systematically absent from the Mt. Ochi veins, having perhaps been obscured during partial recrystallization of the vein quartz.

Natural fractures exhibit a power-law size distribution, whose apertures increase with their length (Vermilye and Scholz 1995; Olson 2003; Alzayer et al. 2015). Whereas narrow veins (< 2 mm) are represented among the Mt. Ochi veins, the highly regular spacing of V_4 veins of similar widths seemingly violates common fracture size distributions. Veins of this width are also frequently assumed to develop from an amalgamation of crack-seal cycles, a conclusion that is elsewhere supported by vein microstructure (Alzayer et al. 2015). As summarized above, several lines of evidence favor a single-seal origin for the Mt. Ochi veins, despite clear support for an initial tensile failure event (i.e., uniform growth of glaucophane along vein walls). The considerable widths of the veins (up to 30 mm) are thus somewhat problematic, particularly given our data which suggest a paragenesis in the middle or lower crust (see below), where elevated confining pressures should limit wall-normal displacement. The extremely high aperture ratios of V_3 veins further complicate matters, with aperture ratios in some veins approaching 1.

The Mt. Ochi veins do, however, exhibit some properties consistent with mechanisms for single-stage vein sealing. 'Contact growth' sealing of Wilson (1994) describes the dynamic recrystallization of vein fill due to stresses imposed by mutual impingement of precipitating crystals during sealing. This may explain, with some limitations, the appearance of strain partitioned entirely into quartz within the veins (see below). Nearby on southern Evia, Nüchter and Stöckhert (2007) interpreted high aperture ratio quartz veins as recording prolonged opening via ductile creep following brittle fracturing linked to seismicity along a structurally higher extensional fault. The veins display evidence for syntaxial sealing, with finer, dynamically recrystallized quartz along vein margins surrounding a progressively coarsening central vein fill. Subsequent numerical modelling of the same veins indicates that the post-seismic widening was accommodated by buckling of the vein walls, with more pronounced widening predicted for vein fill that is more viscous than the surrounding host rock (Nüchter 2017).

Wider Mt. Ochi veins similarly show an increase in grain size from margins to cores; however, the contrast is neither as pronounced nor as consistently developed as the examples described by Nüchter and Stöckhert (2007). Although entire veins appear minimally deformed, quartz in the Mt. Ochi veins exhibits evidence of incipient dynamic recrystallization, in contrast to the undeformed glaucophane and phengite (Fig. S1). Quartz grain boundaries are commonly serrated and interlobate, with low-amplitude bulging and some small new grains formed along grain boundaries (Fig. S2). There is an apparent decrease in recrystallized volume fraction from earliest (V_1) to latest (V_4) veins, although recrystallized volume fraction is known to be sensitive to parameters of probable relevance to the Mt. Ochi veins, including water content and co-active dissolution–precipitation creep (Stipp and Kunze 2008). The textures described are largely consistent with low-temperature grain boundary migration (i.e., bulging of Stipp et al. 2002), with or without minor subgrain rotation, likely at temperatures below ~400 °C. Interpreting the unusual single-increment sealing widths and high apertures via sequential brittle fracture and ductile creep may explain, in part, the recrystallized quartz textures. However, the widening of many parallel veins by ductile mechanisms implies complementary strain should be found in the host rock, for which we observe no evidence. Furthermore, the quartz-dominated veins are predicted to be less viscous relative to the pyroxene-albite host rock, which should be unfavorable to creep-mediated widening according to the models of Nüchter (2017). We accordingly hesitate to comprehensively interpret the opening and sealing mechanisms of the Mt. Ochi veins, but find sufficient microstructural evidence supporting inward-directed crystal growth indicative of a syntaxial sealing mechanism.

The broader structural context of the Mt. Ochi veins alludes to a major rheological control on fracturing. Moreover, the coexistence of mineralogically identical vein sets in several contrasting orientations implies short-term variability of the local stress field. Cyclic redistribution of crustal fluids along pathways created by viscously deforming rock and consequent local pore fluid pressure (P_f) variability commonly governs localization of brittle strain at or below the brittle-ductile transition (e.g., Sibson 1994, 2000; Hayman and Lavier 2014; Behr and Bürgmann 2021; Menegon and Fagereng 2021). As P_f approaches lithostatic conditions, transient changes in the local stress field are also more likely to occur (Faulkner et al. 2006; Ujiie et al. 2018). These stress changes may manifest either as a rotation of the principal stress orientations, or a modified stress ellipsoid (e.g., Scott 1996; Healy 2009).

The Mt. Ochi vein sets define an orthorhombic symmetry (Fig. 1b). The first veins to open, V_1 and V_2, and some V_3 veins, define conjugate sets bisected by the orientations of the more abundant, NNW-SSE striking V_3 veins (Fig. 2a, d). This distribution of vein orientations, seemingly forming relatively quickly, implies instantaneous shortening along the vertical axis with $\sigma_2 \approx \sigma_3$, allowing for instantaneous stretching in a range of directions within the horizontal plane, consistent with an overall oblate stress regime where $\sigma_v = \sigma_1$ (compressive stresses are negative). The latest vein set, V_4, occurs in a comparatively restricted ENE-WSW orientation and cross-cuts all previously formed veins, indicative of a transition to a more prolate stress field. Without a substantial contribution from P_f, this arrangement would require unrealistic tectonic stresses with tensional σ_3 and σ_2. These successive stress states can be attained, however, if P_f varies during vein formation (e.g., Sharma et al. 2023). The earlier vein sets (V_1-V_3) likely formed under a stress regime characterized by $\sigma_1 > P_f > \sigma_2$, creating an oblate effective stress field. Later, V_4 veins opened and sealed following a reduction of P_f such that $\sigma_2 > P_f > \sigma_3$, with V_4 veins consequently opening exclusively perpendicular to σ_3. Since the implied local σ_3 is oriented perpendicular to the ENE-WSW trending mineral lineation (and associated regional stretching lineation; Xypolias et al. 2012), it appears likely that the stress field that produced the Mt. Ochi veins was restricted to the local scale and controlled mainly by P_f fluctuations. High vein concentrations (Fig. 2) may imply that fracture saturation was achieved, perhaps due to enhanced fracture density induced by the rheological relationship of the viscous quartzitic matrix enveloping tabular metabasalt bodies (e.g., Reches 1998). Local saturation of V_3 veins – which are appropriately oriented perpendicular to the regional stretching lineation – may have caused any subsequent fractures to open orthogonal to V_3, matching the observed relationship with V_4 veins (Zulauf et al. 2014).

The quartzites, when ductile, likely acted as fluid conduits, with episodic fracturing in the metabasalt coinciding with fluid redistribution and corresponding P_f changes in the surrounding quartzites. An extensional setting, as implied by the hypothesized stress field described here, is also consistent with our new geochronology (see below). Whereas fluid-mediated hydrofracturing during ductile deformation is most often invoked for veins formed in subduction zones (Hayman and Lavier 2014; Behr and Bürgmann 2021; Menegon and Fagereng 2021), it has also been described from extensional regimes (Nüchter and Ellis 2011; Kassaras et al. 2022). Veins elsewhere in southern Evia have been interpreted as the products of distributed brittle-ductile strain beneath a major detachment fault (Nüchter and Stöckhert 2007), presumably the post-orogenic NCDS. Applying the latter correlation to the Mt. Ochi veins is sensible, given the broad structural similarities between the veins and apparent temporal coincidence with the NCDS (Jolivet et al. 2010). A crucial difference between the Mt. Ochi veins and the apparently coeval veins of Nüchter and Stöckhert (2007) are the absence of glaucophane and high-Si phengite from the latter. Such strikingly contrasting parageneses, despite effectively forming simultaneously, merit additional scrutiny.

Temperatures of crystallization

Quartz and phengite from the Mt. Ochi veins yield consistently positive $\delta^{18}O$ values relative to VSMOW. Phengite data occupy a narrow range between 10.7 and 11.9‰, whereas quartz spans a comparatively wider range between 14.9 and 18.5‰ (Table 2). Quartz-phengite pairs from V_1 and V_4 yield similar T estimates of 335 ± 40 °C and 315 ± 40 °C, respectively, whereas the V_3 quartz-phengite pair returns a significantly lower temperature of 172 ± 40 °C (Zheng 1993). We attribute this discrepancy mainly to the V_3 quartz, as $\delta^{18}O$ of V_3 phengite is within the error of that of V_4 phengite. The elevated $\delta^{18}O$ value obtained for the V_3 quartz aliquot may be due to contamination by quartz that was not in equilibrium with the broader vein system, that is, quartz material inadvertently sampled from the groundmass or from late increments of vein fill. Notably, V_3 exhibits the greatest density of fluid inclusions among the vein generations; however, quartz preferentially incorporates heavy oxygen isotopes relative to aqueous fluids, and contamination by the primary fluid $\delta^{18}O$ is unlikely to produce anomalously high values (Table 2). Thus, solid-phase contamination appears to be the more likely explanation. Due to a lack of petrographic evidence to support later incursion of fluids and associated mineral growth in V_3 veins, we consider it more likely that these high values represent those of the host rocks, which have previously yielded comparably high $\delta^{18}O$ values for quartz (16.6‰; Katzir et al. 2000).

We consider the underlying assumption of isotopic equilibrium between vein-hosted quartz and phengite to be reasonable given the common presence of quartz as inclusions in early marginal glaucophane coexisting with phengite and its presence in the interstices between phengite crystals (Figs. 3d, f, 5a–c). The validity of this assumption is further supported by the consistency between two of the calculated temperatures and those temperatures inferred to have accompanied nascent recrystallization of the vein quartz (< 400 °C) based on microstructures. Quartz-water fractionation calculations after Matsuhisa et al. (1979), using the T determined by quartz-phengite thermometry, indicate the parental fluid had a moderate positive $\delta^{18}O$ signature typical of igneous or metamorphic fluids. Although partial incorporation of a meteoric water signature cannot be discounted outright, any such contribution was likely relatively small and would not have significantly altered fluid chemistry or T. Since magmatism in the Cyclades is broadly late Miocene in age, and thus younger than the veins (see below), we consider the parental fluid to the Mt. Ochi veins to have most likely been of metamorphic origin.

Timing of vein formation

Mt. Ochi vein-hosted phengite and glaucophane yield $^{87}Rb/^{87}Sr$ and $^{40}Ar/^{39}Ar$ dates within error of one another (Fig. 7, 8). *In-situ* $^{87}Rb/^{87}Sr$ data, pooled from all vein sets within each sample (Table 1), define single isochrons providing late Oligocene to earliest Miocene dates. Whereas glaucophane are overwhelmingly Rb-poor and cluster near the $^{87}Sr/^{86}Sr$ axis, they nevertheless fall along isochrons defined by the phengite data alone (Fig. 7 **inset**). This implies that—at minimum with respect to $^{87}Rb/^{87}Sr$ systematics—phengite and glaucophane across all vein sets effectively crystallized coevally, and given their apparent textural equilibrium and co-orientation are likely in isotopic equilibrium, as well. Whether or not the geochronology captures the timing of this crystallization requires an assessment of whether (1) the geochronometers have sustained strain or fluid interaction resulting in recrystallization, and (2) the system experienced T in excess of the nominal closure temperature of either isotope system following vein sealing.

Both the $^{40}Ar/^{39}Ar$ and $^{87}Rb/^{87}Sr$ systems can exhibit strain-sensitive resetting that has been extensively documented, particularly for white mica (e.g., Dunlap et al. 1991; Freeman et al. 1997; Kellett et al. 2016; Barnes et al. 2023; Larson et al. 2023; Ribeiro et al. 2023). In the Cyclades, this often accounts for the young exhumation-related ages recorded by ostensibly HP phengite (e.g., Wijbrans et al. 1990; Bröcker et al. 2004). However, we discount this interpretation for the Mt. Ochi veins for two reasons. The first is that, due to the orthorhombic symmetry of the vein sets, a stress field of any orientation would impose a resolved

shear stress on at least one of the vein orientations. Consequently, if the Mt. Ochi veins recorded any significant strain following sealing, at least one vein set should exhibit evidence of non-coaxial strain such as vein rotation, development of flanking structures, or development of an internal foliation due to transposition of the elongate vein minerals in response to shearing. Only endmember coaxial deformation would not produce such structures, and structures observed in the area show mainly monoclinic symmetries, with strain analysis yielding nonzero W_k, as expected of a strain regime influenced by major regional detachments (Jolivet et al. 2004; Ring et al. 2007b; Xypolias et al. 2010, 2012). Second, the $^{87}Rb/^{87}Sr$ system in phengite has shown greater retentivity, even in strained crystals, compared with corresponding $^{40}Ar/^{39}Ar$ dates (Larson et al. 2023; Ribeiro et al. 2023). Thus, the fact that both geochronometers record the same dates and exhibit no obvious microstructural evidence of recrystallization or significant post-crystallization dissolution-reprecipitation (Fig. 5a-c; Fig. S1) strongly disfavors strain-induced resetting.

Single-grain total fusion $^{40}Ar/^{39}Ar$ dating of vein-hosted phengite provided minimally scattered early Miocene $^{40}Ar/^{39}Ar$ dates that offer the most precise and internally consistent geochronologic constraints (Fig. 8 inset). Glaucophane total fusion data are comparatively scattered and exhibit poor $^{40}Ar/^{39}Ar$ systematics (low $^{40}Ar*$ yields), although many dates are within error of the phengite data, and any interpretation using these dates is equivocal. As previously mentioned, high Ca/K ratios obtained from glaucophane may reflect analysis of an outsized proportion of sodic-calcic rim material or may signal the presence of fluid or solid inclusions (e.g., epidote, titanite). Inclusions commonly act as sinks for Ar, and their presence during analysis results in spurious 'old' apparent ages (Kelley 2002), which likely explains the dispersion in the glaucophane $^{40}Ar/^{39}Ar$ data. Excellent agreement between the phengite $^{40}Ar/^{39}Ar$ data and the $^{87}Rb/^{87}Sr$ isochron dates suggest that these provide a reasonable minimum age for the veins. Textural criteria within the veins combined with quartz-phengite oxygen isotope thermometry support crystallization temperatures of ~315–335°C, below even the minimum closure temperature estimates for either isotope system in phengite (e.g., Bosse et al. 2005; Warren et al. 2012; Laurent et al. 2017). Moreover, peak T estimates for the Ochi Unit (≤ 460 °C; Katzir et al. 2000; Ducharme et al. 2022) likewise approximate or fall below realistic estimates for these closure temperature values. We therefore consider it unlikely that the geochronology reflects cooling and thus conclude that the dates capture the timing of primary crystallization during vein sealing. The phengite $^{40}Ar/^{39}Ar$ data provide the most robust estimates of this timing at *c.* 22–23 Ma. As previously noted, this timing coincides with similar dates throughout the Cyclades that are interpreted to record localized ductile strain below the major detachment systems, and imply a genetic relationship between the veins and the NCDS structurally above.

P–T-X controls on vein paragenesis

Our structural data and geochronology imply that glaucophane and high-Si phengite in the Mt. Ochi veins crystallized in the early Miocene, likely as the rock package was transiting the brittle-ductile transition. Prevailing models for the geodynamic evolution of the eastern Mediterranean suggest that by the early Miocene, the effects of slab rollback had begun influencing the upper crust, creating an incipient back-arc environment and signalling the transition toward the modern, fully extensional tectonic regime (Jolivet and Brun 2010; Ring et al. 2010; van Hinsbergen and Schmid 2012; Jolivet et al. 2013). In the Cyclades, this transition produced deformation below major detachments associated with greenschist to amphibolite facies retrogression of peak HP-LT assemblages, alongside coeval supra detachment basin fill sequences and decompression melting in the central Cyclades (Sanchez-Gomez et al. 2002; Vanderhaeghe et al. 2004; Jolivet et al. 2010; Ring et al. 2010; Grasemann et al. 2012). Accordingly, our data present compelling evidence that glaucophane and phengite in the Mt. Ochi veins crystallized under tectonometamorphic conditions at odds with the HP-LT parageneses conventionally assigned to those minerals.

Although it is tempting to interpret the disparity between expected and apparent metamorphic conditions as reflecting local excursions in *P* or *T*, both are precluded by our new data. Positive pressure anomalies induced by, for example, non-hydrostatic stress states yield equilibrium shifts too modest to account for the assemblages present in the Mt. Ochi veins (e.g., Wheeler 2014; Hess et al. 2022). Competent materials undergoing strain within a rheologically heterogeneous package are moreover expected to behave as compartments of *low* relative pressure (Mancktelow 2008), as are the tensile fractures which here host the HP minerals. Meanwhile, locally cooler *T* may be achieved within a fracture if a cool (i.e., presumably meteoric) throughgoing fluid achieves saturation before thermally equilibrating with its surroundings, but our oxygen isotope data indicate fluid $\delta^{18}O$ signatures more aligned with a metamorphic or magmatic fluid (Table 2). Whereas some influence from small departures in *P* and *T* cannot be precluded, this was likely limited to a complementary role.

Conversely, abundant data have demonstrated that bulk system composition is a critical determinant of whether a blueschist or greenschist facies assemblage develops at particular PT conditions (Guiraud 1982; Maruyama et al. 1986; Massonne and Willmer 2008; Ukar and Cloos 2014; Manzotti et al. 2020; Muñoz-Montecinos et al. 2020). The

stability of Na-amphibole and Na-clinopyroxene extends to considerably lower P if these minerals incorporate sufficient proportions of the Fe^{3+}-rich endmembers (magnesio-)riebeckite and aegirine, respectively (Maruyama et al. 1986; Liu and Bohlen 1995). Amphibole cores and rims as well as clinopyroxene in the metabasaltic host at Mt. Ochi all incorporate > 0.4 mol fraction of their respective ferric endmembers, as well as ferriwinchite in amphibole rims (Fig. 6c-e). Tschermak substitution in white mica is likewise sensitive to elevated fO_2, provided concomitant high α_{SiO2} (Wang et al. 2017), a condition that was undoubtedly satisfied given the large volumes of quartz precipitated alongside the mica. Hematite is abundant in the host lithologies as the sole oxide phase, further attesting to elevated systemic fO_2 above the hematite-magnetite buffer.

The validity of this assumption may be tested using certain compositional geobarometers. Sections of the basaltic host rock which exhibit minimal veining and lack glaucophane comprise predominantly fuzzy clinopyroxene occluded by fine-grained quartz inclusions (Fig. 4). These textures may preserve the earlier prograde conversion of albite to jadeite, for example, in an oceanic plagiogranite protolith (e.g., Miyazaki et al. 1998; Tsujimori and Harlow 2012). Alternately, the inclusions may represent incongruent dissolution of jadeite within an already Si-saturated fluid (e.g., Wohlers et al. 2011). Nevertheless, textural evidence from visibly altered parts of the rock indicates that host rock-fluid interactions locally drove the retrograde conversion of clinopyroxene to albite via the reaction jadeite + quartz → albite (Fig. 3a-b, f), producing also residual hematite from the aegirine component (Fig. 4c). Liu and Bohlen (1995) demonstrated the pressure-dependence of the jadeite + quartz → albite equilibrium on the Fe^{3+} content of clinopyroxene. They calculated, to a lower bound of 10 kbar and 400°C, the stability of clinopyroxene with $X_{jd} = 0.5$. Assuming continuous linear behaviour at still lower T and X_{jd}, the equilibrium extrapolates to ~ 8 kbar at 300°C and perhaps lower still for X_{jd} of 0.4 as encountered in

Table 3 Summary of existing pressure-temperature data from the vicinity of southern Evia

| Locality	Unit	Lithology	Method	Temperature	Pressure	Interpretation	Age	Reference
Southern Evia	Tsakei and Ochi Units (CBU)	Metabasite	Thermocalc v2.5, oxygen isotope thermometry	425 ± 25°C	>11 kbar	M1 (peak, HP)	Eocene	Katzir et al. (2000)
				<350°C	<8 kbar	M2 (retrograde)	Early Miocene	
	Styra and Ochi Units (CBU)	Not specified	Thermocalc v2.3, Si-in-phengite, empirical calculations	400 ± 50°C	11 ± 1 kbar	M1 (peak, HP)	Post-middle Eocene	Shaked et al. (2000)
				380 ± 50°C	6 ± 1 kbar	M2 (retrograde)	-	
	Ochi Unit (CBU)	Glaucophane schist	PERPLE_X	460 ± 20°C	12 ± 1 kbar	Peak, HP	~50 Ma (peak), 30 ± 2 Ma (PT sample $^{40}Ar/^{39}Ar$)	Ducharme et al. (2022)
	Basal Unit	Pumpellyite-albite schist		310 ± 15 °C	7 ± 1 kbar	Retrograde	26 ± 1 Ma	
Lavrion (SE Attica)	Lavrion schists (CBU)	Mica schist	white mica-chlorite thermobarometry	311 ± 34°C	11 ± 2 kbar	M1 (peak, HP)	32-23 Ma	Scheffer et al. (2016); geochronology from Coleman et al. (2019)
				311 ± 34°C	7.5 ± 1.5 kbar	M3 (retrograde)		
	Kamariza schists (CBU)			298 ± 38°C	9.5 ± 1.5 kbar	M1 (peak, HP)	22-8 Ma	
				345 ± 40°C	6.75 ± 1.75 kbar	M3 (retrograde)		
Andros	Cycladic Blueschist Unit	Mica schist	white mica-chlorite thermobarometry	260-400°C	8-14 kbar	Syn-orogenic exhumation	Pre-37 Ma	Huet et al. (2015)
				260-460°C	7 ± 1 kbar	Isobaric heating	Pre-30 Ma	
				410 ± 20°C	4-8 kbar	Post-orogenic exhumation	Pre-21 Ma	
	Makrotantalon Unit	Garnet-glaucophane schist	Theriak-Domino	550°C	18.5 kbar	Peak, HP	50-40 Ma	
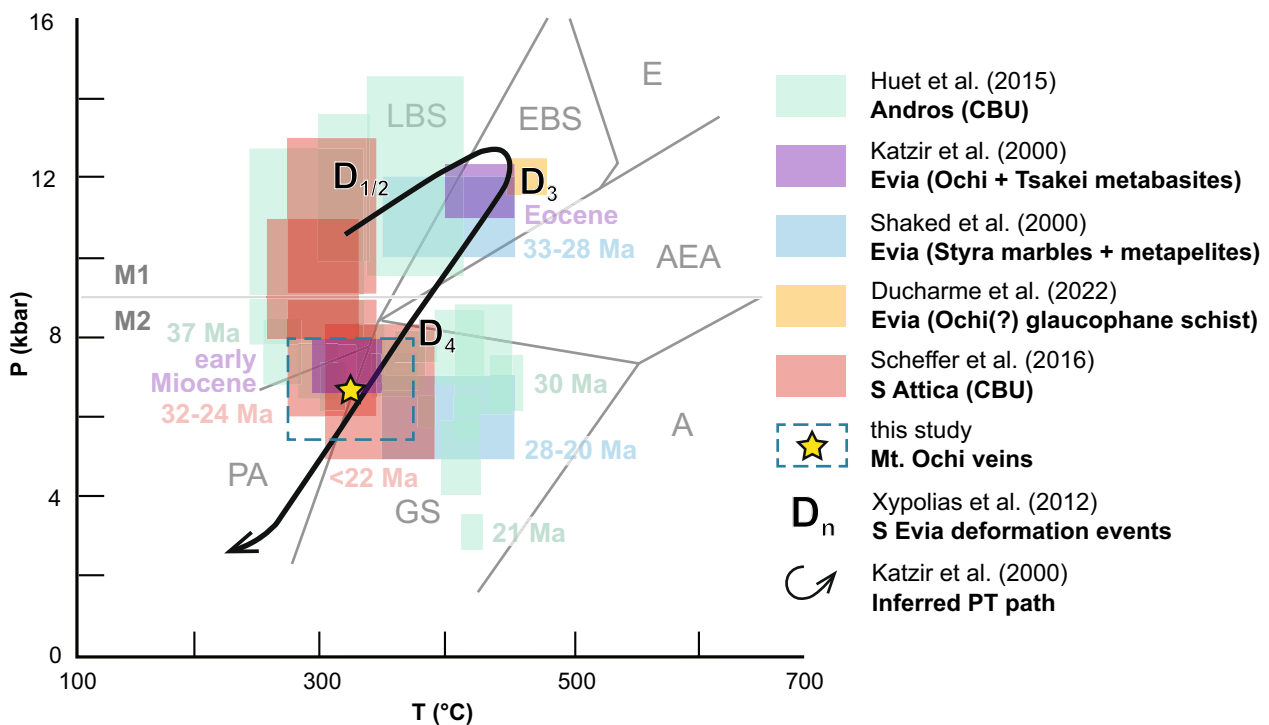
Fig. 9 Pressure–temperature (PT) diagram summarizing previous estimates for metamorphic conditions and their approximate timing from the vicinity of southern Evia. Metamorphism recorded by the Cycladic Blueschist Unit (CBU) can be broadly subdivided into M1 (high pressure-low temperature) and M2 (retrograde greenschist facies), which fall approximately to either side of ~9 kbar. Further details for each PT estimate are provided in Table 3. Facies boundaries after Evans (1990)

the Mt. Ochi metabasalts. Maruyama et al. (1986) described an alternative geobarometer using Al_2O_3 contents of Na-amphibole for systems with coexisting chlorite having X_{Fe} of 0.4–0.5, similar to the chlorite described here. A graphical estimate of core, mantle, and rim P estimates for the vein-hosted glaucophane vary from ~5.5–6 kbar (6–8 wt.% Al_2O_3), ~6–7 kbar (7–9 wt.% Al_2O_3), and ~4 kbar (2–3 wt.% Al_2O_3), respectively. The relatively low pressures indicated by these estimates are supported by high X_{Ps} epidote compositions (with $Fe^{3+}/(Fe^{3+} + Al)$ corresponding to X_{Ps} of 0.28–0.32; Maruyama et al. 1986), which are in textural equilibrium with the glaucophane, phengite, and albite.

Notably, even the Na-amphibole species closest to end-member glaucophane in the Mt. Ochi veins is predicted to be stable at conditions generally associated with greenschist facies assemblages in the Cyclades. Such high-P greenschist facies parageneses are widely documented along retrograde segments of the clockwise PT paths in the region (e.g., Parra et al. 2002; Huet et al. 2015; Scheffer et al. 2016; Ducharme et al. 2022). Aggregation of petrogenetic modelling data has led to a proposal that the CBU had a protracted residence near the blueschist-greenschist facies transition resulting in isobaric heating during a pause in its unroofing history

(Parra et al. 2002; Huet et al. 2015; Laurent et al. 2018; Peillod et al. 2021). This cessation occurred at greater apparent depths toward the central Cyclades, commensurate with the deeper structural levels exhumed there. Evia is proximal to Andros, which Huet et al. (2015) suggested experienced this arrest at 7 ± 1 kbar, in agreement with the P estimates calculated above. Our estimates of PT conditions during vein formation are effectively identical to those previously determined for retrograde assemblages in the CBU and structurally lower units on southern Evia (Katzir et al. 2000; Ducharme et al. 2022; Fig. 9, Table 3), and to those interpreted to record the end of syn-orogenic exhumation on Andros (Huet et al. 2015). The new data imply a crustal geothermal gradient between 11 and 17 °C/km at *c.* 22–23 Ma, comparable to the 16–17 °C/km gradient inferred from the essentially synchronous (*c.* 21 Ma) onset of post-orogenic extension on Tinos (Parra et al. 2002; Tirel et al. 2009). Therefore, although the empirical geobarometers applied above yield some apparent inconsistency with the assumption of a single increment of vein sealing, the consistency with existing regional data strongly suggests the *P* and *T* estimates are reasonable. The apparent and abrupt shifts in *P* implied by Al_2O_3 contents may allude to rapid fluctuations in bulk

composition during vein sealing, perhaps by consequence of sluggish kinetics of jadeite-fluid reactions at these relatively low temperatures, or due to fractionation of a stagnant fluid (e.g., Oliver and Bons 2001; Schott et al. 2009).

In summary, the Mt. Ochi veins likely developed at PT conditions more commonly associated with greenschist facies, rather than blueschist facies, assemblages throughout the CBU. Bulk composition of the system was likely primarily responsible for the favored crystallization of nominally 'blueschist facies' minerals. A direct control on the mineral assemblage was exerted by high Na contents (mediated by host rock clinopyroxene) and fO_2 (mediated by the through-going fluid) and the resultant predominance of ferric iron within the system, as demonstrated for rock subducted only to near the greenschist-blueschist facies boundary (Manzotti et al. 2020; Muñoz-Montecinos et al. 2020). Contrasting with those previous examples, the Mt. Ochi veins apparently developed some ~ 20–30 Myr following peak HP metamorphism, after substantial unroofing of the Ochi Unit had already occurred. This conclusion implies that certain mineral assemblages routinely used to empirically validate data as relating to subduction zone geodynamics may conversely capture conditions coinciding with exhumation. Additional caution should be exerted when designing projects to study subduction-related tectonic processes, particularly heeding the Fe^{3+} content of HP clinopyroxene and amphibole species in rocks selected for these purposes.

Fluid source and modes of solute transport

Models for atypical silicate veins commonly invoke either local diffusive mass transfer from adjacent host rock or advection from an external source (e.g., Kerrick 1990; Beitter et al. 2008). Local diffusion is often favored due to physical limitations on establishing hydrothermal circulation at a regional scale. Metamorphic vein minerals typically co-occur as host rock porphyroblasts in these systems, offering petrological evidence supporting the same conclusion (Kerrick 1990). Advective transport implies significant fluid volumes exploiting an extensive permeability network, affording a short interval over which a fluid may deposit its solutes. The local volumetric density and limited extent of the Mt. Ochi veins, as well as the occurrence of chemically indistinguishable phengite and amphibole in the host rock, favor a proximal source.

Glaucophane and phengite in the veins, however, exhibit essentially proportional Fe and Mg (X_{Mg}: 0.50–0.74 and 0.45–0.61, respectively), whereas clinopyroxene in the host rock contains little or no Mg (< 5 wt.%; mean: 1.8 wt.%). Similarly, no primary sources of Ca or K were identified in either host lithotype. Compositional homogeneity of the vein and host rock minerals suggests a shared genesis related to the vein-forming fluid. Other phases in textural equilibrium

with glaucophane and phengite, including chlorite and epidote, likewise incorporated these components and are likely, therefore, hydrothermal. Thus, the only hydrous minerals observed in either host lithotype are apparently part of a metasomatic assemblage that includes glaucophane + phengite + epidote + chlorite + hematite + quartz. The fluid was accordingly either generated by primary hydrous minerals that are now entirely obscured or else was externally derived. We consider the latter option more compelling, and accordingly conclude that the Mt. Ochi veins are most likely the products of coupled short-range diffusion and long-range advection.

Katzir et al. (2000) attributed geochemical features of the Ochi metabasalts and gabbros to seafloor alteration of primary alkalic petrogenetic features, including elevated Na, K, and Fe, depleted Ca, and the presence of aegirine-rich Na-clinopyroxene. These authors also invoked a nappe-scale hydrothermal system during peak HP metamorphism to account for enriched $\delta^{18}O$ signatures of the glaucophane in these rocks. The geochemical features proposed to be fingerprints of a seafloor hydrothermal system bear a striking resemblance to the fluid components implicated here in producing the Mt. Ochi glaucophane-phengite veins. Vein-hosted quartz and phengite also exhibit elevated $\delta^{18}O$ signatures like those Katzir et al. (2000) associate with peak HP-LT conditions, which they concluded were derived from a fluid in equilibrium with Ochi Unit metasediments. Because our conclusions broadly align with those of Katzir et al. (2000), we propose that their inferred large-scale hydrothermal system was the same system responsible for the Mt. Ochi veins. Rather than operating at peak burial, however, these fluids produced far-reaching metasomatic alteration of the metabasites during syn-exhumation metamorphism near the blueschist-greenschist facies transition (Fig. 9). Whereas Katzir et al. (2000) considered the aegirine-rich clinopyroxene to be a primary magmatic artifact, our documentation of increasing aegirine component toward clinopyroxene rims in the metasomatized host rock argues instead that initially jadeitic clinopyroxene was converted to more aegirine-rich compositions with greater degrees of fluid interaction.

The paragenesis of a single vein set can be summarized as follows. Initially small volumes of a Si-saturated, oxidized K- and Mg-bearing aqueous fluid infiltrate the metabasite, perhaps channelized by adjacent viscously deforming quartzite (Fig. 10a). Vein minerals preferentially nucleate on, and crystallize inward from, the wall rock, while reactions between the Si-rich fluids and jadeite in the host rock may liberate additional components to drive the crystallization of glaucophane and phengite. The positive ΔV of the jadeite + quartz → albite reaction, once proceeding in a sufficient volume of the rock, may promote further fracturing (Fig. 10b). Later sealing increments of a given vein are
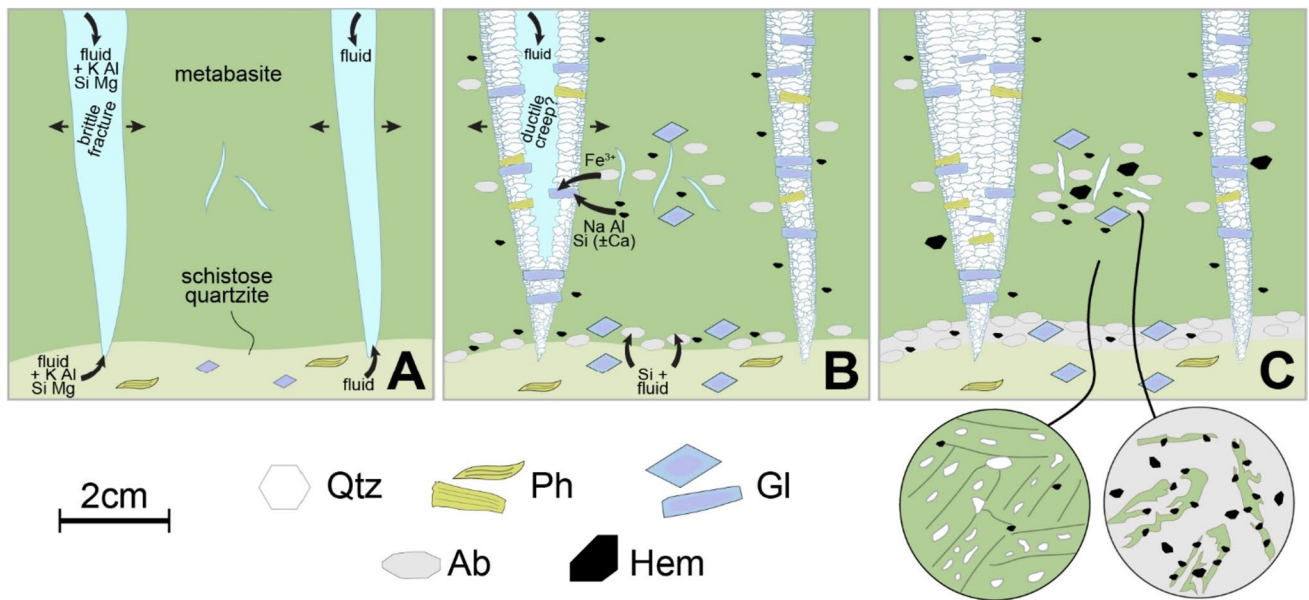
Fig. 10 Schematic diagram depicting the development of a single Mt. Ochi vein set. **A** Initial fracture formation. Fluids infiltrate metabasaltic layers following channeling in ductilely deforming schistose quartzite, infilling fractures and pre-existing pore space in the host rock. **B** The modified bulk composition introduced by the fluids promotes the growth of glaucophane, phengite, and hematite, as well as the conversion of jadeite to albite. A subset of the veins are selected to widen, possibly via ductile creep mechanisms. Later increments of sealing are comparatively dominated by quartz, with lower modal propor-tions of the ferromagnesian phases observed along the vein walls. **C** The second (or later) increment of vein fill, comprising comparatively quartz-rich, glaucophane- and phengite-poor precipitates, yields the final sealed state of the vein(s). Albite-rich layers form at interfaces between the metabasalt and schistose quartz, due to greater proximity of fluid, shorter diffusion length-scales for reaction with silica, or both. Callout bubbles in C show the detail of well-preserved clinopyroxene domains (poikiloblasts) compared with fluidized albite-bearing domains (skeletal with hematite overgrowths)

dominated by quartz with comparatively sparse phengite and glaucophane (Fig. 10c).

Limited available thermodynamic data for aqueous solubilities, speciation, and activities of silicate minerals as well as computational demands currently prohibit comprehensive modeling of the paragenesis of the Mt. Ochi veins (Tiraboschi et al. 2018; Macris et al. 2020; Menzel et al. 2020). Microstructures observed in jadeite, along with its high aqueous solubility among silicates (Azimov and Burin 2007), implicate dissolution and reactive conversion to albite as possible mechanisms for local contributions to vein mineral growth. Structurally and chemically simple minerals (e.g., Al_2SiO_5 polymorphs) predominate as vein fill in metamorphic veins (e.g., Kerrick 1990; Beitter et al. 2008; Bucholz and Ague 2010), suggesting that these are thermodynamically favored over comparatively complex minerals like glaucophane and phengite.

Whether the relevant control on the precipitation of these minerals in the Mt. Ochi veins has bearing on apparently disparate P recorded in zoned amphibole (Fig. 9), which in a single-sealing model has grown continuously without variations in ambient metamorphic conditions, relies on more data than presently available for the governing thermodynamic mechanisms. The Mt. Ochi veins nonetheless provide an exceptional snapshot of reactive transport processes in operation and may serve as ideal natural analogues with which to test the conclusions of future theoretical and experimental predictions.

Conclusions

Glaucophane- and phengite-bearing quartz veins from Mt. Ochi on southernmost Evia island record (micro-)structural, geochronological, and stable isotope evidence that mutually support crystallization during vein sealing at lower pressures than typically predicted for nominally HP minerals. Fracturing styles and the consistent subvertical orientation of σ_1 indicate opening and single-increment sealing within an extensional stress field. Miocene $^{87}Rb/^{87}Sr$ and $^{40}Ar/^{39}Ar$ dates corroborate the structural data, demonstrating that the nominally HP minerals crystallized at a time widely perceived to coincide with back-arc extension and greenschist facies retrograde metamorphism throughout the Aegean. Oxidizing fluids accomplished advective redistribution of material from relatively local sources, likely within the same structural unit, alongside diffusion from the host rock.

The structural alignment of HP minerals, like glaucophane, is widely used to assign an early, syn-convergence timing to associated structures and fabrics within the overall tectonometamorphic evolution of an orogen (e.g., Inger and Cliff 1994; Wintsch et al. 1999; Rosenbaum et al. 2002; Xypolias et al. 2012; Augier et al. 2015; Corti et al. 2017). These inferences are predicated on the paradigm that blueschist and eclogite facies assemblages survive only where the influence of post-peak, syn-exhumation strain and fluidization is minimal (e.g., Fitzherbert et al. 2005; Halama and Konrad-Schmolke 2015; Roche et al. 2016), or where fluid compositions favor their preservation (Kleine et al. 2014). Our data reinforce observations that natural mineral assemblages widely associated with HP-LT conditions may in fact have formed at relatively shallow depths (Manzotti et al. 2020; Muñoz-Montecinos et al. 2020), and newly extend these observations to the retrograde path. Accordingly, inferences based only on the presence of minerals like glaucophane in the field may be meaningless in the context of syn-convergent tectonics.

Declaration

References

Alzayer Y, Eichhubl P, Laubach SE (2015) Non-linear growth kinematics of opening-mode fractures. J Struct Geol 74:31–44. https://doi.org/10.1016/j.jsg.2015.02.003

Armbruster T, Bonazzi P, Akasaka M et al (2006) Recommended nomenclature of epidote-group minerals. Eur J Mineral 18(5):551–567. https://doi.org/10.1127/0935-1221/2006/0018-0551

Augier R, Jolivet L, Gadenne L, Lahfid A, Driussi O (2015) Exhumation kinematics of the cycladic blueschists unit and back-arc extension, insight from the Southern Cyclades (Sikinos and Folegandros Islands, Greece). Tectonics 34(1):152–185. https://doi.org/10.1002/2014TC003664

Azimov PY, Bushmin SA (2007) Solubility of minerals of metamorphic and metasomatic rocks in hydrothermal solutions of varying acidity: thermodynamic modeling at 400–800°C and 1–5 kbar. Geochem Int 45:1210–1234. https://doi.org/10.1134/S0016702907120038

Barnes CJ, Schneider DA, Majka J, Camacho A, Bukała M, Włodek A (2023) ^{40}Ar/^{39}Ar dates controlled by white mica deformation and strain localization: Insights from comparing in situ laser ablation and single-grain fusion techniques. J Metamorph Geol 41(9):1143–1166. https://doi.org/10.1111/jmg.12739

Bebout GE, Barton MD (1993) Metasomatism during subduction: products and possible paths in the Catalina Schist. California Chem Geol 108(1–4):61–92. https://doi.org/10.1016/0009-2541(93)90318-D

Behr WM, Bürgmann R (2021) What's down there? The structures, materials and environment of deep-seated slow slip and tremor. Philosophical Transactions of the Royal Society A, 379(2193):20200218 https://doi.org/10.31223/osf.io/tyzb9

Beitter T, Wagner T, Markl G (2008) Formation of kyanite–quartz veins of the Alpe Sponda, Central Alps, Switzerland: implications for Al transport during regional metamorphism. Contrib Mineral Petrol 156(6):689–707. https://doi.org/10.1007/s00410-008-0310-4

Bons PD (2001) The formation of large quartz veins by rapid ascent of fluids in mobile hydrofractures. Tectonophysics 336(1–4):1–17. https://doi.org/10.1016/S0040-1951(01)00090-7

Bons PD, Elburg MA, Gomez-Rivas E (2012) A review of the formation of tectonic veins and their microstructures. J Struct Geol 43:33–62. https://doi.org/10.1016/j.jsg.2012.07.005

Bosse V, Féraud G, Ballèvre M, Peucat JJ, Corsini M (2005) Rb–Sr and ^{40}Ar/^{39}Ar ages in blueschists from the Ile de Groix (Armorican Massif, France): Implications for closure mechanisms in isotopic systems. Chem Geol 220(1–2):21–45. https://doi.org/10.1016/j.chemgeo.2005.02.019

Bröcker M, Bieling D, Hacker B, Gans P (2004) High-Si phengite records the time of greenschist facies overprinting: Implications for models suggesting mega-detachments in the Aegean Sea. J Metamorph Geol 22(5):427–442. https://doi.org/10.1111/j.1525-1314.2004.00524.x

Bucholz CE, Ague JJ (2010) Fluid flow and Al transport during quartz-kyanite vein formation, Unst, Shetland Islands. Scotland J Metamorph Geol 28(1):19–39. https://doi.org/10.1111/j.1525-1314.2009.00851.x

Bukała M, Barnes CJ, Jeanneret P, Hidas K, Mazur S, Almqvist BS, Kośmińska K, Klonowska I, Šurka J, Majka J (2020) Brittle deformation during eclogitization of early Paleozoic blueschist. Front Earth Sci 8:594453. https://doi.org/10.3389/feart.2020.594453

Castelli D, Rolfo F, Compagnoni R, Xu S (1998) Metamorphic veins with kyanite, zoisite and quartz in the Zhu-Jia-Chong eclogite, Dabie Shan. China Island Arc 7(1–2):159–173. https://doi.org/10.1046/j.1440-1738.1998.00185.x

Cawthorn RG, Collerson KD (1974) The recalculation of pyroxene end-member parameters and the estimation of ferrous and ferric iron content from electron microprobe analyses. Am Miner J Earth Planet Mater 59(11–12):1203–1208

Coleman M, Dubosq R, Schneider DA, Grasemann B, Soukis K (2019) Along-strike consistency of an extensional detachment system, West Cyclades, Greece. Terra Nova 31(3):220–233. https://doi.org/10.1111/ter.12388

Corti L, Alberelli G, Zanoni D, Zucali M (2017) Analysis of fabric evolution and metamorphic reaction progress at Lago della Vecchia-Valle d'Irogna, Sesia-Lanzo Zone. Western Alps J Maps 13(2):521–533. https://doi.org/10.1080/17445647.2017.1331177

Cossette É, Schneider DA, Warren CJ, Grasemann B (2015) Lithological, rheological, and fluid infiltration control on $^{40}Ar/^{39}Ar$ ages in polydeformed rocks from the West Cycladic detachment system. Greece Lithosphere 7(2):189–205. https://doi.org/10.1130/L416.1

Ducharme TA, Schneider DA, Grasemann B, Klonowska I (2022) Stretched thin: Oligocene extrusion and ductile thinning of the Basal Unit along the Evia Shear Zone, NW Cyclades, Greece. Tectonics 41(12):e2022TC007561 https://doi.org/10.1029/2022TC007561

Dunlap WJ, Teyssier C, McDougall I, Baldwin S (1991) Ages of deformation from K/Ar and $^{40}Ar/^{39}Ar$ dating of white micas. Geology 19(12):1213–1216. https://doi.org/10.1130/0091-7613(1991)019%3c1213:AODFKA%3e2.3.CO;2

Dürr ST, Altherr R, Keller JO, Okrusch MM, Seidel E (1978) The median Aegean crystalline belt: Stratigraphy, structure, metamorphism, magmatism. In: Cloos H, Roeder D, Schmidt K (eds) Alps, Apennines, Hellenides 38. Schweizerbart, Stuttgart, pp 455–477

Evans BW (1990) Phase relations of epidote-blueschists. Lithos 25(1–3):3–23. https://doi.org/10.1016/0024-4937(90)90003-J

Faulkner DR, Mitchell TM, Healy D, Heap MJ (2006) Slip on "weak" faults by the rotation of regional stress in the fracture damage zone. Nature 444(7121):922–925. https://doi.org/10.1038/nature05353

Fitzherbert JA, Clarke GL, Powell R (2005) Preferential retrogression of high-P metasediments and the preservation of blueschist to eclogite facies metabasite during exhumation, Diahot terrane. NE New Caledonia Lithos 83(1–2):67–96. https://doi.org/10.1016/j.lithos.2005.01.005

Freeman SR, Inger S, Butler RWH, Cliff RA (1997) Dating deformation using Rb-Sr in white mica: Greenschist facies deformation ages from the Entrelor shear zone. Italian Alps Tectonics 16(1):57–76. https://doi.org/10.1029/96TC02477

Gao J, Klemd R (2001) Primary fluids entrapped at blueschist to eclogite transition: evidence from the Tianshan meta-subduction complex in northwestern China. Contrib Mineral Petrol 142(1):1–14. https://doi.org/10.1007/s004100100275

Gerogiannis N, Xypolias P, Chatzaras V, Aravadinou E, Papapavlou K (2019) Deformation within the Cycladic subduction–exhumation channel: new insights from the enigmatic Makrotantalo nappe (Andros, Aegean). Int J Earth Sci 108:817–843. https://doi.org/10.1007/s00531-019-01680-3

Giuntoli F, Viola G (2022) A likely geological record of deep tremor and slow slip events from a subducted continental broken formation. Sci Rep 12(1):4506. https://doi.org/10.1038/s41598-022-08489-2

Govindaraju K (1979) Report (1968–1978) on two mica reference samples: biotite Mica-Fe and phlogopite Mica-Mg. Geostand Newsl 3(1):3–24. https://doi.org/10.1111/j.1751-908X.1979.tb00235.x

Grasemann B, Schneider DA, Stöckli DF, Iglseder C (2012) Miocene divergent crustal extension in the Aegean: Evidence from the western Cyclades (Greece). Lithosphere 4(1):23–39. https://doi.org/10.1130/L164.1

Guiraud M (1982) Géothermobarométrie du faciès schiste vert à glaucophane: modélisation et applications (Afghanistan, Pakistan, Corse, Bohême). Dissertation, University of Montpellier

Halama R, Konrad-Schmolke M (2015) Retrograde metasomatic effects on phase assemblages in an interlayered blueschist-greenschist sequence (Coastal Cordillera, Chile). Lithos 216:31–47. https://doi.org/10.1016/j.lithos.2014.12.004

Harlov DE, Austrheim H (2013) Metasomatism and the chemical transformation of rock: rock-mineral-fluid interaction in terrestrial and extraterrestrial environments. In: Harlov DE, Austrheim H (eds) Metasomatism and the Chemical Transformation of Rock. Lecture Notes in Earth System Sciences, Springer Berlin Heidelberg, pp 1–16 https://doi.org/10.1007/978-3-642-28394-9_1

Hawthorne FC, Oberti R, Harlow GE, Maresch WV MRF, Schumacher JC, Welch MD (2012) Nomenclature of the amphibole supergroup. Am Miner 97(11–12):2031–2048. https://doi.org/10.2138/am.2012.4276

Hayman NW, Lavier LL (2014) The geologic record of deep episodic tremor and slip. Geology 42(3):195–198. https://doi.org/10.1130/G34990.1

Healy D (2009) Anisotropy, pore fluid pressure and low angle normal faults. J Struct Geol 31(6):561–574. https://doi.org/10.1016/j.jsg.2009.03.001

Hess BL, Ague JJ, Voorhees PW (2022) Quantifying the effects of non-hydrostatic stress on multi-component minerals. J Geophys Res Solid Earth 127(9):e2022JB025201 https://doi.org/10.1029/2022JB025201

Hogmalm KJ, Zack T, Karlsson AKO, Sjöqvist AS, Garbe-Schönberg D (2017) In situ Rb–Sr and K-Ca dating by LA-ICP-MS/MS: an evaluation of N_2O and SF_6 as reaction gases. J Anal Atomic Spectrom 32(2):305–313. https://doi.org/10.1039/C6JA00362A

Huang F, Sverjensky DA (2019) Extended Deep Earth Water Model for predicting major element mantle metasomatism. Geochim Cosmochim Acta 254:192–230. https://doi.org/10.1016/j.gca.2019.03.027

Huet B, Labrousse L, Monie P, Malvoisin B, Jolivet L (2015) Coupled phengite $^{40}Ar-^{39}Ar$ geochronology and thermobarometry: PTt evolution of Andros Island (Cyclades, Greece). Geol Mag 152(4):711–727 https://doi.org/10.1017/S0016756814000661

Inger S, Cliff RA (1994) Timing of metamorphism in the Tauern Window, Eastern Alps: Rb-Sr ages and fabric formation. J Metamorph Geol 12(5):695–707. https://doi.org/10.1111/j.1525-1314.1994.tb00052.x

Jacobshagen V (1986) Geologie von Griechland. Borntraeger, Berlin-Stuttgart

Jolivet L, Brun JP (2010) Cenozoic geodynamic evolution of the Aegean. Int J Earth Sci 99(1):109–138. https://doi.org/10.1007/s00531-008-0366-4

Jolivet L, Lecomte E, Huet B et al (2010) The north cycladic detachment system. Earth Planet Sci Lett 289(1–2):87–104. https://doi.org/10.1016/j.epsl.2009.10.032

Jolivet L, Faccenna C, Huet B et al (2013) Aegean tectonics: Strain localisation, slab tearing and trench retreat. Tectonophysics 597:1–33. https://doi.org/10.1016/j.tecto.2012.06.011

Jolivet L, Famin V, Mehl C, Parra T, Aubourg C, Hébert R, Philippot P (2004) Strain localization during crustal-scale boudinage to form extensional metamorphic domes in the Aegean Sea. In: Whitney DL, Teyssier C, Siddoway CS, Gneiss domes in orogeny. Geological Society of America Special Papers, Colorado, pp 185–210 https://doi.org/10.1130/0-8137-2380-9.185

Kassaras I, Kapetanidis V, Ganas A et al (2022) Seismotectonic analysis of the 2021 Damasi-Tyrnavos (Thessaly, Central Greece) earthquake sequence and implications on the stress field rotations. J Geodyn 150:101898. https://doi.org/10.1016/j.jog.2022.101898

Katsikatsos G (1991a) Geological map of Greece, Karystos sheet. Institute of Geological Mining Research (IGME), Athens

Katsikatsos G (1991b) Geological map of Greece, Aliveri sheet. Institute of Geological Mining Research (IGME), Athens

Katzir Y, Avigad D, Matthews A, Garfunkel Z, Evans BW (2000) Origin, HP/LT metamorphism and cooling of ophiolitic mélanges in southern Evia (NW Cyclades). Greece J Metamorph Geology

18(6):699–718. https://doi.org/10.1046/j.1525-1314.2000.00281.x

Kellett DA, Warren C, Larson KP, Zwingmann H, van Staal CR, Rogers N (2016) Influence of deformation and fluids on Ar retention in white mica: Dating the Dover Fault, Newfoundland Appalachians. Lithos 254:1–17. https://doi.org/10.1016/j.lithos.2016.03.003

Kelley S (2002) Excess argon in K-Ar and Ar-Ar geochronology. Chem Geol 188(1–2):1–22. https://doi.org/10.1016/S0009-2541(02)00064-5

Kerrick DM (1990) Aluminum metasomatism. In: Ribbe PH (ed) The Al_2SiO_5 polymorphs. Rev Miner 22:311–352.

Kleine BI, Skelton AD, Huet B, Pitcairn IK (2014) Preservation of blueschist-facies minerals along a shear zone by coupled metasomatism and fast-flowing CO_2-bearing fluids. J Petrol 55(10):1905–1939. https://doi.org/10.1093/petrology/egu045

Larson KP, Button M, Shrestha S, Camacho A (2023) A comparison of $^{87}Rb/^{87}Sr$ and $^{40}Ar/^{39}Ar$ dates: evaluating the problem of excess ^{40}Ar in Himalayan mica. Earth Planet Sci Lett 609:118058. https://doi.org/10.1016/j.epsl.2023.118058

Laurent V, Beaudoin A, Jolivet L, Arbaret L, Augier R, Rabillard A, Menant A (2015) Interrelations between extensional shear zones and synkinematic intrusions: the example of Ikaria Island (NE Cyclades, Greece). Tectonophysics 651:152–171. https://doi.org/10.1016/j.tecto.2015.03.020

Laurent V, Huet B, Labrousse L, Jolivet L, Monie P, Augier R (2017) Extraneous argon in high-pressure metamorphic rocks: Distribution, origin and transport in the Cycladic Blueschist Unit (Greece). Lithos 272:315–335. https://doi.org/10.1016/j.lithos.2016.12.013

Laurent V, Lanari P, Naïr I, Augier R, Lahfid A, Jolivet L (2018) Exhumation of eclogite and blueschist (Cyclades, Greece): Pressure–temperature evolution determined by thermobarometry and garnet equilibrium modelling. J Metamorph Geol 36(6):769–798. https://doi.org/10.1111/jmg.12309

Laurent V, Scaillet S, Jolivet L, Augier R, Roche V (2021) ^{40}Ar behaviour and exhumation dynamics in a subduction channel from multi-scale $^{40}Ar/^{39}Ar$ systematics in phengite. Geochim Cosmochim Acta 311:141–173. https://doi.org/10.1016/j.gca.2021.06.001

Liu J, Bohlen SR (1995) Mixing properties and stability of jadeite-acmite pyroxene in the presence of albite and quartz. Contrib Mineral Petrol 119:433–440. https://doi.org/10.1007/BF00286940

Locock AJ (2014) An Excel spreadsheet to classify chemical analyses of amphiboles following the IMA 2012 recommendations. Comput Geosci 62:1–11. https://doi.org/10.1016/j.cageo.2013.09.011

Macris CA, Newton RC, Wykes J, Pan R, Manning CE (2020) Diopside, enstatite and forsterite solubilities in H_2O and H_2O-NaCl solutions at lower crustal and upper mantle conditions. Geochim Cosmochim Acta 279:119–142. https://doi.org/10.1016/j.gca.2020.03.035

Maluski H, Vergely P, Bavay D, Bavay P, Katsikatsos G (1981) $^{39}Ar/^{40}Ar$ dating of glaucophanes and phengites in southern Euboa (Greece); geodynamic implications. Bull Geol Soc France 7(5):469–476. https://doi.org/10.2113/gssgfbull.S7-XXIII.5.469

Mancktelow NS (2008) Tectonic pressure: Theoretical concepts and modelled examples. Lithos 103(1–2):149–177. https://doi.org/10.1016/j.lithos.2007.09.013

Manzotti P, Ballèvre M, Pitra P, Putlitz B, Robyr M, Müntener O (2020) The growth of sodic amphibole at the greenschist-to-blueschist-facies transition (Dent Blanche, Western Alps): bulk-rock chemical control and thermodynamic modelling. J Petrol 61(4):egaa044 https://doi.org/10.1093/petrology/egaa044

Maruyama S, Cho M, & Liou JG (1986) Experimental investigations of blueschist-greenschist transition equilibria: Pressure dependence

of Al_2O_3 contents in sodic amphiboles—a new geobarometer. In: Evans BW, Brown HB (eds) Blueschists and Eclogites. Mem Geol Soc Am 164:1–16 https://doi.org/10.1130/MEM164-p1

Massonne HJ, Willner AP (2008) Phase relations and dehydration behaviour of psammopelite and mid-ocean ridge basalt at very-low-grade to low-grade metamorphic conditions. Eur J Miner 20(5):867–879. https://doi.org/10.1127/0935-1221/2008/0020-1871

Matsuhisa Y, Goldsmith JR, Clayton RN (1979) Oxygen isotopic fractionation in the system quartz-albite-anorthite-water. Geochim Cosmochim Acta 43(7):1131–1140. https://doi.org/10.1016/0016-7037(79)90099-1

Mehl C, Jolivet L, Lacombe O, Labrousse L, Rimmele G (2007) Structural evolution of Andros (Cyclades, Greece): a key to the behaviour of a (flat) detachment within an extending continental crust. Geol Soc Lond Spec Pub 291(1):41–73. https://doi.org/10.1144/SP291.3

Menant A, Jolivet L, Augier R, Skarpelis N (2013) The North Cycladic Detachment System and associated mineralization, Mykonos, Greece: Insights on the evolution of the Aegean domain. Tectonics 32(3):433–452. https://doi.org/10.1002/tect.20037

Menegon L, Fagereng Å (2021) Tectonic pressure gradients during viscous creep drive fluid flow and brittle failure at the base of the seismogenic zone. Geology 49(10):1255–1259. https://doi.org/10.1130/G49012.1

Menzel MD, Garrido CJ, Sánchez-Vizcaíno VL (2020) Fluid-mediated carbon release from serpentinite-hosted carbonates during dehydration of antigorite-serpentinite in subduction zones. Earth Planet Sci Lett 531:115964. https://doi.org/10.1016/j.epsl.2019.115964

Miyazaki K, Sopaheluwakan J, Zulkarnain I, Wakita K (1998) A jadeite–quartz–glaucophane rock from Karangsambung, central Java. Indonesia Island Arc 7(1–2):223–230. https://doi.org/10.1046/j.1440-1738.1998.00164.x

Muñoz-Montecinos J, Angiboust S, Cambeses A, García-Casco A (2020) Multiple veining in a paleo–accretionary wedge: the metamorphic rock record of prograde dehydration and transient high pore-fluid pressures along the subduction interface (Western Series, central Chile). Geosphere 16(3):765–786. https://doi.org/10.1130/GES02227.1

Nüchter JA (2017) How vein sealing boosts fracture widening rates—the buckling-enhanced aperture growth mechanism for syn-tectonic veins. Tectonophysics 694:69–86. https://doi.org/10.1016/j.tecto.2016.11.005

Nüchter JA, Ellis S (2010) Complex states of stress during the normal faulting seismic cycle: role of midcrustal postseismic creep. J Geophys Res Solid Earth 115(B12):411. https://doi.org/10.1029/2010JB007557

Nüchter JA, Stöckhert B (2007) Vein quartz microfabrics indicating progressive evolution of fractures into cavities during postseismic creep in the middle crust. J Struct Geol 29(9):1445–1462. https://doi.org/10.1016/j.jsg.2007.07.011

Oliver NH, Bons PD (2001) Mechanisms of fluid flow and fluid–rock interaction in fossil metamorphic hydrothermal systems inferred from vein–wallrock patterns, geometry and microstructure. Geofluids 1(2):137–162. https://doi.org/10.1046/j.1468-8123.2001.00013.x

Olson JE (2003) Sublinear scaling of fracture aperture versus length: an exception or the rule? J Geophys Res Solid Earth 108(B9):2413. https://doi.org/10.1029/2001JB000419

Papanikolaou D (2009) Timing of tectonic emplacement of the ophiolites and terrane paleogeography in the Hellenides. Lithos 108(1–4):262–280. https://doi.org/10.1016/j.lithos.2008.08.003

Parra T, Vidal O, Jolivet L (2002) Relation between the intensity of deformation and retrogression in blueschist metapelites of Tinos

Island (Greece) evidenced by chlorite–mica local equilibria. Lithos 63(1–2):41–66. https://doi.org/10.1016/S0024-4937(02)00115-9

Peillod A, Majka J, Ring U, Drüppel K, Patten C, Karlsson A, Włodek A, Tehler E (2021) Differences in decompression of a high-pressure unit: A case study from the Cycladic Blueschist Unit on Naxos Island. Greece Lithos 386:106043. https://doi.org/10.1016/j.lithos.2021.106043

Philippot P, Selverstone J (1991) Trace-element-rich brines in eclogitic veins: Implications for fluid composition and transport during subduction. Contrib Mineral Petrol 106:417–430. https://doi.org/10.1007/BF00321985

Ramsay JG (1980) The crack–seal mechanism of rock deformation. Nature 284(5752):135–139. https://doi.org/10.1016/0191-8141(80)90038-3

Ramsay JG, Huber MI (1983) The techniques of modern structural geology, Vol 1: strain analysis. Academic Press, Cambridge

Reches ZE (1998) Tensile fracturing of stiff rock layers under triaxial compressive stress states. Int J Rock Mech Min Sci 35(4–5):456–457. https://doi.org/10.1016/S0148-9062(98)00086-2

Ribeiro BV, Kirkland CL, Kelsey DE, Reddy SM, Hartnady MI, Faleiros FM, Rankenburg K, Liebmann J, Korhonen FJ, Clark C (2023) Time-strain evolution of shear zones from petrographically constrained Rb–Sr muscovite analysis. Earth Planet Sci Lett 602:117969. https://doi.org/10.1016/j.epsl.2022.117969

Ring U, Glodny J, Will T, Thomson S (2007b) An Oligocene extrusion wedge of blueschist-facies nappes on Evia, Aegean Sea, Greece: implications for the early exhumation of high-pressure rocks. J Geol Soc 164(3):637–652. https://doi.org/10.1144/0016-76492006-041

Ring U, Glodny J, Will T, Thomson S (2010) The Hellenic subduction system: high-pressure metamorphism, exhumation, normal faulting, and large-scale extension. Ann Rev Earth Planet Sci 38:45–76. https://doi.org/10.1146/annurev.earth.050708.170910

Ring U, Will T, Glodny J, Kumerics C, Gessner K, Thomson S, Güngör T, Monié P, Okrusch M, Drüppel K (2007a) Early exhumation of high-pressure rocks in extrusion wedges: Cycladic blueschist unit in the eastern Aegean, Greece, and Turkey. Tectonics 26(2) https://doi.org/10.1029/2005TC001872

Roche V, Laurent V, Cardello GL, Jolivet L, Scaillet S (2016) Anatomy of the Cycladic Blueschist Unit on Sifnos Island (Cyclades, Greece). J Geodyn 97:62–87. https://doi.org/10.1016/j.jog.2016.03.008

Rösel D, Zack T (2022) LA-ICP-MS/MS Single-Spot Rb-Sr Dating. Geostand Geoanal Res 46(2):143–168. https://doi.org/10.1111/ggr.12414

Rosenbaum G, Avigad D, Sánchez-Gómez M (2002) Coaxial flattening at deep levels of orogenic belts: evidence from blueschists and eclogites on Syros and Sifnos (Cyclades, Greece). J Struct Geol 24(9):1451–1462. https://doi.org/10.1016/S0191-8141(01)00143-2

Sanchez-Gomez M, Avigad D, Heimann A (2002) Geochronology of clasts in allochthonous Miocene sedimentary sequences on Mykonos and Paros Islands: implications for back-arc extension in the Aegean Sea. J Geol Soc 159(1):45–60. https://doi.org/10.1144/0016-764901031

Scheffer C, Vanderhaeghe O, Lanari P, Tarantola A, Ponthus L, Photiades A, France L (2016) Syn-to post-orogenic exhumation of metamorphic nappes: Structure and thermobarometry of the western Attic-Cycladic metamorphic complex (Lavrion, Greece). J Geodyn 96:174–193. https://doi.org/10.1016/j.jog.2015.08.005

Schliestedt M, Matthews A (1987) Transformation of blueschist to greenschist facies rocks as a consequence of fluid infiltration, Sifnos (Cyclades). Greece Contrib Mineral Petrol 97(2):237–250. https://doi.org/10.1007/BF00371243

Schneider DA, Senkowski C, Vogel H, Grasemann B, Iglseder C, Schmitt AK (2011) Eocene tectonometamorphism on Serifos (western Cyclades) deduced from zircon depth-profiling geochronology and mica thermochronology. Lithos 125(1–2):151–172. https://doi.org/10.1016/j.lithos.2011.02.005

Schott J, Pokrovsky OS, Oelkers EH (2009) The link between mineral dissolution/precipitation kinetics and solution chemistry. Rev Miner Geochem 70(1):207–258. https://doi.org/10.2138/rmg.2009.70.6

Scott DR (1996) Seismicity and stress rotation in a granular model of the brittle crust. Nature 381(6583):592–595. https://doi.org/10.1038/381592a0

Shaked Y, Avigad D, Garfunkel Z (2000) Alpine high-pressure metamorphism at the Almyropotamos window (southern Evia, Greece). Geol Mag 137(4):367–380 https://doi.org/10.1017/S001675680000426X

Sharma NK, Biswal TK, Chinnasamy SS (2023) Structural implications of paleofluid pressure and paleostress estimates of the quartz veins from sulfide deposits of the Ambaji-Deri region, Neoproterozoic South Delhi Terrane, Aravalli-Delhi Mobile Belt. North-West India J Asian Earth Sci 245:105552. https://doi.org/10.1016/j.jseaes.2023.105552

Sibson RH (1994) Crustal stress, faulting and fluid flow. Geol Soc Lond Spec Pub 78(1):69–84. https://doi.org/10.1144/GSL.SP.1994.078.01.07

Sibson RH (2000) Tectonic controls on maximum sustainable overpressure: fluid redistribution from stress transitions. J Geochem Explor 69:471–475. https://doi.org/10.1016/S0375-6742(00)00090-X

Spandler C, Hermann J (2006) High-pressure veins in eclogite from New Caledonia and their significance for fluid migration in subduction zones. Lithos 89(1–2):135–153. https://doi.org/10.1016/j.lithos.2005.12.003

Stipp M, Kunze K (2008) Dynamic recrystallization near the brittle-plastic transition in naturally and experimentally deformed quartz aggregates. Tectonophysics 448(1–4):77–97. https://doi.org/10.1016/j.tecto.2007.11.041

Stipp M, Stünitz H, Heilbronner R, Schmid SM (2002) The eastern Tonale fault zone: a 'natural laboratory' for crystal plastic deformation of quartz over a temperature range from 250 to 700 °C. J Struct Geol 24(12):1861–1884. https://doi.org/10.1016/S0191-8141(02)00035-4

Tiraboschi C, Tumiati S, Sverjensky D, Pettke T, Ulmer P, Poli S (2018) Experimental determination of magnesia and silica solubilities in graphite-saturated and redox-buffered high-pressure COH fluids in equilibrium with forsterite + enstatite and magnesite + enstatite. Contrib Mineral Petrol 173:1–17. https://doi.org/10.1007/s00410-017-1427-0

Tirel C, Gautier P, Van Hinsbergen DJJ, Wortel MJR (2009) Sequential development of interfering metamorphic core complexes: numerical experiments and comparison with the Cyclades. Greece Geol Soc Lond Spec Pub 311(1):257–292. https://doi.org/10.1144/SP311.10

Tomaschek F, Kennedy AK, Villa IM, Lagos M, Ballhaus C (2003) Zircons from Syros, Cyclades, Greece—recrystallization and mobilization of zircon during high-pressure metamorphism. J Petrol 44(11):1977–2002. https://doi.org/10.1093/petrology/egg067

Tsujimori T, Harlow GE (2012) Petrogenetic relationships between jadeitite and associated high-pressure and low-temperature metamorphic rocks in worldwide jadeitite localities: a review. Eur J Miner 24(2):371–390. https://doi.org/10.1127/0935-1221/2012/0024-2193

Ujiie K, Saishu H, Fagereng Å, Nishiyama N, Otsubo M, Masuyama H, Kagi H (2018) An explanation of episodic tremor and slow slip constrained by crack-seal veins and viscous shear in subduction

mélange. Geophys Res Lett 45(11):5371–5379. https://doi.org/10.1029/2018GL078374

Ukar E, Cloos M (2014) Low-temperature blueschist-facies mafic blocks in the Franciscan mélange, San Simeon, California: Field relations, petrology, and counterclockwise P-T paths. GSA Bull 126(5–6):831–856. https://doi.org/10.1130/B30876.1

Urai JL, Williams PF, Van Roermund HLM (1991) Kinematics of crystal growth in syntectonic fibrous veins. J Struct Geol 13(7):823–836. https://doi.org/10.1016/0191-8141(91)90007-6

Uunk B, Brouwer F, de Paz-Álvarez M, van Zuilen K, Huybens R, van't Veer R, Wijbrans J (2022) Consistent detachment of supracrustal rocks from a fixed subduction depth in the Cyclades. Earth Planet Sci Lett 584:117479 https://doi.org/10.1016/j.epsl.2022.117479

Uysal IT, Feng YX, Zhao JX, Bolhar R, Işik V, Baublys KA, Yago A, Golding SD (2011) Seismic cycles recorded in late Quaternary calcite veins: geochronological, geochemical and microstructural evidence. Earth Planet Sci Lett 303(1–2):84–96. https://doi.org/10.1016/j.epsl.2010.12.039

van Hinsbergen DJ, Schmid SM (2012) Map view restoration of Aegean–West Anatolian accretion and extension since the Eocene. Tectonics 31(5) https://doi.org/10.1029/2012TC003132

Vanderhaeghe O (2004) Structural development of the Naxos migmatite dome. In: Whitney DL, Teyssier C, Siddoway CS (eds) Gneiss Domes in Orogeny. Geol Soc Am Spec Pap 378:211–228 https://doi.org/10.1130/0-8137-2380-9.211

Vermeesch P (2018) IsoplotR: A free and open toolbox for geochronology. Geosci Front 9(5):1479–1493. https://doi.org/10.1016/j.gsf.2018.04.001

Vermilye JM, Scholz CH (1995) Relation between vein length and aperture. J Struct Geol 17(3):423–434. https://doi.org/10.1029/98JB00957

Wang R, Cudahy T, Laukamp C et al (2017) White mica as a hyperspectral tool in exploration for the Sunrise Dam and Kanowna Belle gold deposits. Western Australia Econ Geol 112(5):1153–1176. https://doi.org/10.5382/econgeo.2017.4505

Warren CJ, Hanke F, Kelley SP (2012) When can muscovite $^{40}Ar/^{39}Ar$ dating constrain the timing of metamorphic exhumation? Chem Geol 291:79–86. https://doi.org/10.1016/j.chemgeo.2011.09.017

Wheeler J (2014) Dramatic effects of stress on metamorphic reactions. Geology 42(8):647–650. https://doi.org/10.1130/G35718.1

Widmer T, Thompson AB (2001) Local origin of high pressure vein material in eclogite facies rocks of the Zermatt-Saas Zone. Switzerland Am J Sci 301(7):627–656. https://doi.org/10.2475/ajs.301.7.627

Wijbrans JR, Schliestedt M, York D (1990) Single grain argon laser probe dating of phengites from the blueschist to greenschist transition on Sifnos (Cyclades, Greece). Contrib Mineral Petrol 104:582–593. https://doi.org/10.1007/BF00306666

Wilson CJL (1994) Crystal growth during a single-stage opening event and its implications for syntectonic veins. J Struct Geol 16(9):1283–1296. https://doi.org/10.1016/0191-8141(94)90070-1

Wintsch RP, Byrne T, Toriumi M (1999) Exhumation of the Sanbagawa blueschist belt, SW Japan, by lateral flow and extrusion: evidence from structural kinematics and retrograde PTt paths. Geol Soc Lond Spec Pub 154(1):129–155. https://doi.org/10.1144/GSL.SP.1999.154.01.06

Wohlers A, Manning CE, Thompson AB (2011) Experimental investigation of the solubility of albite and jadeite in H_2O, with paragonite + quartz at 500 and 600 °C, and 1–2.25 GPa. Geochim Cosmochim Acta 75(10):2924–2939 https://doi.org/10.1016/j.gca.2011.02.028

Xypolias P, Spanos D, Chatzaras V, Kokkalas S, Koukouvelas I (2010) Vorticity of flow in ductile thrust zones: examples from the Attico-Cycladic Massif (Internal Hellenides, Greece). Geol Soc Lond Spec Pub 335(1):687–714. https://doi.org/10.1144/SP335.28

Xypolias P, Iliopoulos I, Chatzaras V, Kokkalas S (2012) Subduction- and exhumation-related structures in the Cycladic Blueschists: Insights from south Evia Island (Aegean region, Greece). Tectonics 31(2) https://doi.org/10.1029/2011TC002946

Zack T, Hogmalm KJ (2016) Laser ablation Rb/Sr dating by online chemical separation of Rb and Sr in an oxygen-filled reaction cell. Chem Geol 437:120–133. https://doi.org/10.1016/j.chemgeo.2016.05.027

Zheng YF (1993) Calculation of oxygen isotope fractionation in hydroxyl-bearing silicates. Earth Planet Sci Lett 120(3–4):247–263. https://doi.org/10.1016/0012-821X(93)90243-3

Zulauf J, Zulauf G, Göttlich J, Peinl M (2014) Formation of chocolate-tablet boudins: Results from scaled analogue models. J Struct Geol 68:97–111. https://doi.org/10.1016/j.jsg.2014.09.005